

Connecting the Deep Collection of Sinking Particles With Surface Ocean Signatures

 Lu Wang¹ , Jonathan Gula^{2,3} , Jérémy Collin¹, Laurent Mémerly¹ , and Xiaolong Yu^{4,5} 

¹Laboratoire des Sciences de l'Environnement Marin (LEMAR), CNRS, IRD, Ifremer, IUEM, University Brest, Plouzané, France, ²Laboratoire d'Océanographie Physique et Spatiale (LOPS), CNRS, IRD, Ifremer, IUEM, University Brest, Plouzané, France, ³Institut Universitaire de France (IUF), Paris, France, ⁴School of Marine Sciences, Sun Yat-sen University, Zhuhai, China, ⁵Guangdong Provincial Key Laboratory of Marine Resources and Coastal Engineering, Zhuhai, China

Key Points:

- The variability of deep-ocean conservative particle collection shows imprints of upper-ocean flow structures in the source regions
- Mesoscale eddies and fronts can induce sharp spatial gradients in particle collection at depth over weekly to monthly time scales
- The heterogeneity of particle collection at depth shows seasonality related to upper-ocean mesoscale eddy activity and frontal development

Supporting Information:

Supporting Information may be found in the online version of this article.

Correspondence to:

X. Yu,
yuxlong5@mail.sysu.edu.cn

Citation:

Wang, L., Gula, J., Collin, J., Mémerly, L., & Yu, X. (2025). Connecting the deep collection of sinking particles with surface ocean signatures. *Journal of Geophysical Research: Oceans*, 130, e2024JC021777. <https://doi.org/10.1029/2024JC021777>

Received 2 SEP 2024

Accepted 9 JUN 2025

Author Contributions:

Formal analysis: Lu Wang

Investigation: Lu Wang

Methodology: Jonathan Gula,

Jérémy Collin

Supervision: Jonathan Gula,

Laurent Mémerly

Writing – original draft: Lu Wang

Writing – review & editing: Lu Wang,

Jonathan Gula, Laurent Mémerly,

Xiaolong Yu

Abstract A major pathway in the biological carbon pump is the gravitational sinking of organic particles from the sunlit ocean (0–200 m) to the deep ocean. Variability in particle fluxes measured by sediment traps is often attributed to variability in primary production in the surface ocean. However, particle fluxes are also influenced by physical processes such as mesoscale eddies and fronts. In this study, we assess the impact of upper-ocean dynamical structures on the variability of particle collection in the deep ocean. This is achieved by forward tracking the trajectories of 51.9 million virtual particles that were homogeneously released at a depth of 200 m with a constant sinking velocity of 50 m d⁻¹ in the Northeast Atlantic basin. We found that, despite a homogeneous particle source without biological effects, purely dynamical changes can induce heterogeneity in particle density and origin at depth. The position of sediment traps can thus significantly influence the weekly to seasonal particle collection in the deep ocean. Additionally, we identify and characterize nine particle clusters using a machine-learning approach. The results show that the seasonality of particle collection at depth can be induced by seasonal variations in upper-ocean flow structures. Clusters associated with eddy and frontal structures are found to intermittently contribute more than 50% of the particle amount during winter and spring, with smaller secondary peaks in the summer months. This study highlights the connection between mesoscale ocean dynamics and the spatio-temporal pattern of conservative (non-biological) particle collection in the deep ocean.

Plain Language Summary Oceanic plants convert atmospheric CO₂ into organic carbon in the form of particles. These particles sink from the surface ocean to the deep ocean by gravity and are often collected by fixed containers in the water column to measure long-term particle fluxes. Such measurements are also influenced by the motions of surrounding seawater, including swirling currents and filamentous structures. This study assesses the impact of these upper-ocean structures on the dynamics of particle collection in space and time by analyzing the trajectories of virtual particles. In the flow field generated by a numerical ocean model, a large number of particles are uniformly seeded at a depth of 200 m and finally reach a fixed zone at 1,000 m. Our findings reveal that the physical motions of seawater can lead to graded changes in particle collection within the deep-ocean target zone. Based on specific traits or attributes of particle trajectories, we classify particles into nine groups, each associated with different flow structures. The seasonal variations in particle amounts across these groups align with the seasonally changing oceanic motions, particularly the swirls and filaments that are most active during winter and spring.

1. Introduction

The biological carbon pump exports particulate organic carbon (POC) from the surface ocean to drive the carbon storage in the deep ocean. It is a multifaceted system driven by a suite of processes. The predominant mechanism is the gravitational settling of organic particles, which was estimated to account for 70% of the total global carbon export (Nowicki et al., 2022). However, the export flux highly depends on the particle size and characteristics. Discrepancies between the carbon export fluxes and those derived from geochemical tracers suggest alternative mechanisms that contribute to deep-sea carbon storage (Emerson, 2014). These additional export pathways include physically mediated (by subduction or mixed layer swallowing) and biologically mediated (by large mesopelagic migrators), which can export all classes of particles (Boyd et al., 2019). The export flux is size-

differentiated as the dominant mechanism can switch from gravitationally driven to advectively driven when the vertical velocity of the flow field is large (Dever et al., 2021).

The delivery of POC to the deep ocean has been investigated using deep-moored sediment traps since the late 1970s. The particle flux recorded at a given location and depth depends on a combination of biological, biogeochemical and physical processes that vary in time and space. Previous studies suggest that the spatial heterogeneity of carbon export is driven by biogeochemical differences (e.g., phytoplankton biomass and nutrient supply) among different flow structures, such as fronts, eddy cores and edges. Heterogeneous biological distributions in the ocean are evident from remote sensing of ocean color (Mahadevan, 2016). This biological patchiness is mostly due to patterned circulation such as frontal systems, mesoscale variability, and coastal upwelling. In particular, mesoscale eddies are known to have a fundamental influence on the transport of materials and dynamical quantities in the global oceans. Horizontal stirring associated with eddies and filaments is found to structure the spatiotemporal organization of the phytoplankton community into (sub-)mesoscale patches (10–100 km) of dominant types (d'Ovidio et al., 2010). A series of direct observations have revealed particle flux events associated with eddy-eddy fronts (Guidi et al., 2012), the edges of a mesoscale cyclonic eddy (Estapa et al., 2019), and cyclonic eddies at different stages of evolution (Zhou et al., 2020). Carbon export within a cyclonic eddy was found to be 2 to 3 times higher than that measured in adjacent ambient waters in the Lee of Hawaii (Bidigare et al., 2003). Low oxygen concentrations in deep waters (1,000 m) suggested higher POC flux events prior to the sampling, despite the low upper ocean carbon export observed in eddies in the oligotrophic North Atlantic Ocean (Buesseler et al., 2008). Thus, carbon export in an energetic eddy field is sensitive to the spatial and temporal variability of the mesoscale activity.

A key finding from moored sediment trap studies has been the seasonality of the particle flux to the deep ocean. The seasonality was generally attributed to the seasonal change in surface primary production with peaks in early spring and lows in late autumn (Deuser et al., 1981; Deuser & Ross, 1980; Honjo, 1982), despite interannual variability in the timing, duration, and magnitude of the seasonal peak (Conte et al., 2001). It has been suggested that predictions of particle export flux can be derived from phytoplankton biomass and net primary production estimated from satellite observations combined with food-web models (Siegel et al., 2014). However, the temporal variability of downward particle flux differentiates particles with different origins and transport histories. In situ observations of POC flux at the long-term abyssal monitoring site Station M in the California Current Ecosystem revealed the importance of episodic intense pulses linked to rapid sinking of salp fecal pellets (Smith et al., 2018) or horizontal advection of highly productive coastal waters (Ruhl et al., 2020). The export flux was found to be decoupled from net primary production at the mesoscale due to temporal and spatial shifts in export, especially in spring when frontal and eddy dynamics are more active (McGillicuddy et al., 2019). Guidi et al. (2007) suggests the importance of mesoscale activity for the seasonal variability of surface carbon export to the mesopelagic layer. The indicator of mesoscale activity, Eddy Kinetic Energy (EKE), is highly variable in time, due to wind work (Wunsch, 1998), baroclinic instability affected by local heating/cooling (Qiu et al., 2008), and the seasonal changes in the energy cascade from the submesoscale to the mesoscale (Naveira Garabato et al., 2022; Schubert et al., 2020, 2023; Yu et al., 2024). As an important mediator of mesoscale kinetic energy transfer, submesoscale motions are well recognized, with stronger intensity in winter and weaker intensity in summer (Callies et al., 2015; Rocha et al., 2016; Shcherbina et al., 2013), leading to a maximum of mesoscale EKE in late spring and early summer.

From a physical perspective, sinking particles are prone to hydrodynamic effects, which should be taken into account when interpreting sediment trap measurements. Over a long period of time, sediment traps continuously sample particles originating from distances as far as hundreds of kilometers away. Studies on the statistical funnels of sediment traps illustrate the variability of the particle source area due to horizontal advection (Siegel & Deuser, 1997; Siegel et al., 1990, 2008; Wang et al., 2022; Waniek et al., 2000). The local presence of eddies and fronts is episodic and can affect the high-frequency variability of the carbon fluxes induced by hydrodynamic processes. The mesoscale activity may also be responsible for regional differences between particle trapping zones during long-term observations. Advective processes often alter the spatial pattern of surface signal transfer to the deep ocean. Thus, lateral transport of particles from productive areas may dominate local surface production signals. Consequently, the seasonal and interannual variability of particle fluxes is partially governed by physical processes rather than solely by local primary production in the overlying euphotic zone (Waniek et al., 2005).

This study aims to investigate how spatial and temporal variability in mesoscale dynamics within the mesopelagic layer (200–1,000 m) affects the heterogeneity of particle distribution at depth, with potential implications for

particle export to the deep ocean. The variability of export production is thought to be mainly determined by biology, although dynamics partially constrain it. We aim to show that the variability of particles sampled at depth, which is purely due to mesoscale and submesoscale dynamics, should be taken into account, a point that has never been clearly addressed. In this work, the “export” is specifically defined as particles originating from 200 m depth that finally reach a collection region at 1,000 m. With an assumption of homogeneous particle production at the surface and by initially focusing solely on physical processes, this study does not explicitly consider biological production or physical-biological interactions. To examine spatial variability and seasonality in deep-ocean particle collection, we analyze forward-tracking trajectories of particles that are initialized homogeneously across a broad surface ocean area. We use key features of these trajectories and metrics of flow structures along them to connect deep-ocean particle collection with upper-ocean dynamics. Given that the heterogeneous dispersion of oceanic materials in space and time is associated with specific flow features, we apply clustering analysis to particle trajectory data to link the main patterns of the deep-ocean particle distributions to hydrodynamic properties.

The paper is organized as follows. Section 2 describes the Lagrangian particle seeding experiments and investigates the heterogeneity of the deep-ocean particle collection. Section 3 presents the clustering method, identifies particle clusters, and links the spatial variability at depth with surface signatures via clustering. Section 4 shows the seasonality of the deep-ocean particle collection in terms of clusters. Finally, conclusions and perspectives for future work are presented in Section 5.

2. Deep-Ocean Particle Collection

2.1. Lagrangian Particle Seeding Experiments

We conducted offline forward particle tracking experiments in the region surrounding the Porcupine Abyssal Plain Sustained Observatory (PAP-SO, 49°N, 16.5°W), a long-term time series site in the Northeast Atlantic Ocean (Hartman et al., 2012; Lampitt et al., 2023). The physical model outputs used for simulations are instantaneous outputs at 12 hourly intervals from the Coastal and Regional Ocean COmmunity model (CROCO) based on ROMS (Shchepetkin & McWilliams, 2005). This model configuration has been described and validated in several studies (Le Corre et al., 2020; Smilenova et al., 2020; Wang et al., 2022). It covers the North Atlantic Subpolar Gyre with 2000×1600 grid points at a horizontal grid spacing of 2 km. The 2 km resolution is much smaller than the first Rossby deformation radius over this region (10–30 km) (Chelton et al., 1998), and thus the model is expected to be eddy-resolving and submesoscale-permitting. The region surrounding PAP-SO is characterized by weak mean flow and moderate eddy kinetic energy, representative of a substantial fraction of the global ocean (Allen & Naveira-Garabato, 2013). Nonetheless, the mesoscale eddy activity in this region is still considerable, with the frequent formation or propagation of coherent mesoscale vortices (X. Zhang et al., 2024). The model does not include tidal forcing, which significantly reduces the generation of internal waves and high-frequency variability.

The Lagrangian particle tracking was performed using a Python/Fortran hybrid parallelized code called “Pyticles” (Gula & Collin, 2021), with the same numerical options described in Wang et al. (2022), where several sensitivity tests have been performed. We define here a 200×200 km target zone centered on the PAP site for particle collection at a depth of 1,000 m. Only particles that eventually reach this target zone are included in the analysis. The particle sinking velocity was set to 50 m d^{-1} , which is a good compromise between the realistic range of sinking velocity and the ability to reflect the influence of flow dynamics. Since this study focuses on the mesopelagic layer (200–1,000 m), a seeding depth of 200 m was chosen to represent the depth at which organic matter is exported. Particles were initialized at grid points on a 1200×1200 km seeding patch centered on the southwest of the PAP site (Figure 1a). The size and center of the seeding patch were determined by backtracking particles from the boundary and center of a 200×200 km collection zone at 2,000 m. This patch ensures complete coverage of the deep target zone at 1,000 m by particles sinking from the export depth. The continuous injection of particles every 12 hr for 7 years (2002–2008) generated more than 2.5 billion particle trajectories. A total of 51,900,650 particles reached the target zone, with approximately 9,000 particles entering at each time step. Figure 1b shows the distribution of particle source locations binned into $10 \text{ km} \times 10 \text{ km}$ grids at 200 m seeding depth, with particle counts reaching up to 10^6 per grid. The target zone primarily collects particles seeded within 500 km radius of the PAP site, with most particles originating no more than 200 km from the site, as indicated by the orange area ($>10^4$ particles in each bin) on the map.

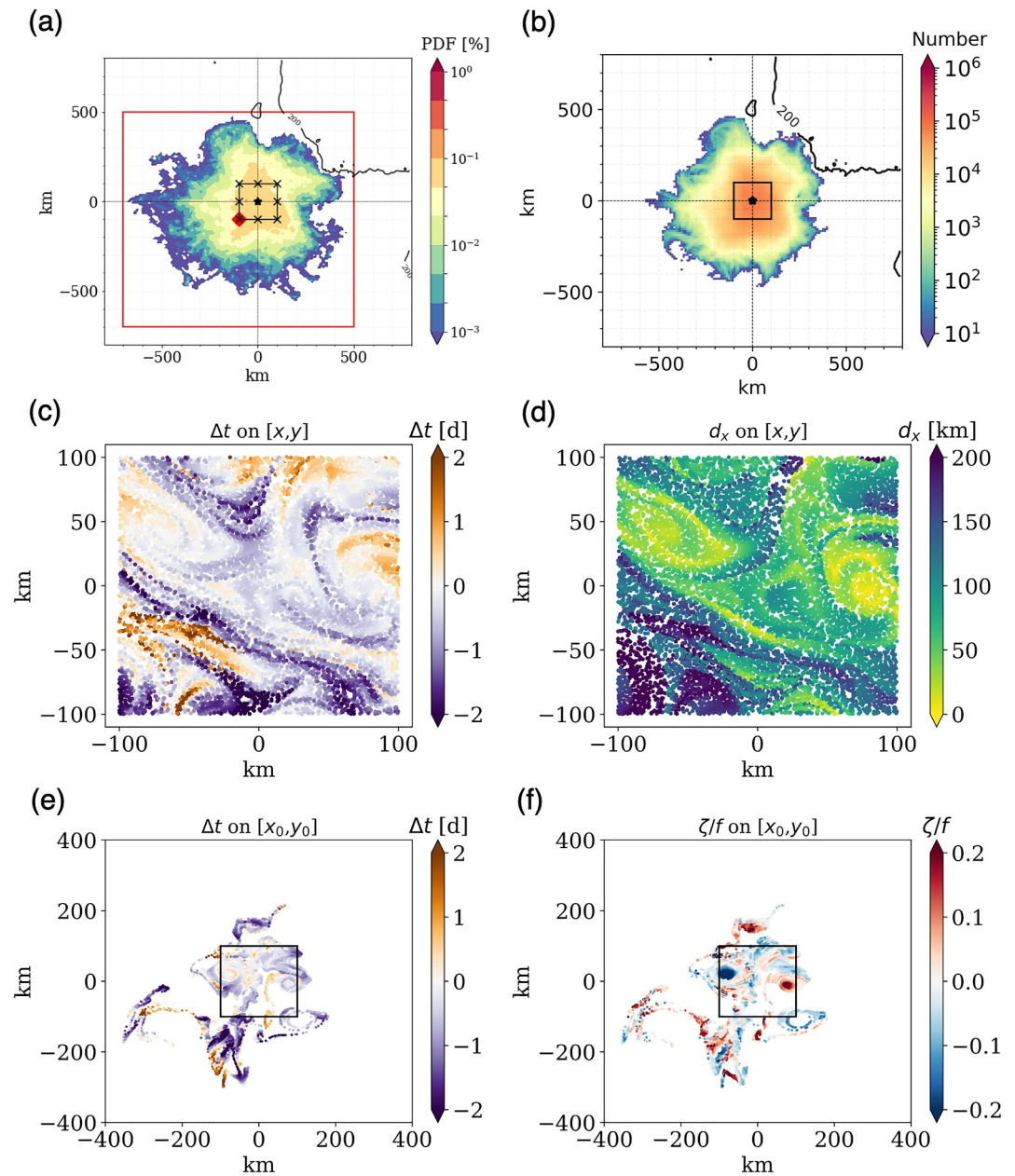


Figure 1. (a) Distribution of particles from the 9 seeding patches on the boundaries and center of a 200×200 km target zone at 2,000 m backtracked to 200 m during the 7 years. The black markers show the centers of 9 backward seeding patches, while the red diamond marks the center of the forward seeding patch southwest of the PAP site. The red square confines the initial seeding patch used for forward simulations. (b) Source locations of 51.9 million particles collected in the 200×200 km target zone at 1,000 m in the 7-year simulation, selected for clustering analysis. Particle positions at 200 m depth are binned into $10 \text{ km} \times 10 \text{ km}$ grids, the black square is the target zone with the PAP site in the center shown as the black star. (c)–(f) Maps of variables for particles reaching the target zone, 50 days after seeding. Travel time anomaly and horizontal displacement mapped on particle final positions in the target zone (c)–(d). Travel time anomaly and relative vorticity mapped on particle initial positions at 200 m depth (e)–(f). The black box in panel (e) marks the area shown in panels (c) and (d).

The original trajectory output consists of particle coordinates in three dimensions as well as velocity data. From the particle trajectories, we compute three fundamental quantities: the horizontal displacement d_x , the length of the particle trajectory $\sum \Delta x$, and the travel time anomaly Δt . The horizontal displacement d_x refers to the horizontal distance between the initial position of the particles in the seeding patch at 200 m and their final position in the target zone at 1,000 m. The trajectory length $\sum \Delta x$ is the cumulative horizontal distance traveled by the particles,

integrated over each time step. The travel time anomaly Δt is defined as the difference between the actual particle travel time and the standard sinking time, assuming no influence of vertical currents. To relate the particle distribution to different flow structures, we also interpolate physical parameters of the Eulerian flow field along the particle trajectories. The four physical quantities are the Okubo-Weiss parameter ($OW = \sigma^2 - \zeta^2$), the relative vorticity ($\zeta = v_x - u_y$), the strain ($\sigma = \sqrt{(u_x - v_y)^2 + (v_x + u_y)^2}$), and the divergence ($\delta = u_x + v_y$).

2.2. Heterogeneity in the Deep-Ocean Particle Collection

When particle fluxes measured by sediment traps are used to assess the biological carbon pump, flux analysis is often performed over longer time scales, such as several months or a year. However, the typical sampling duration of sediment traps ranges from about 1 week to 1 month, and a few hours to one day during cruises. The limited size of sediment traps makes it impossible to sample a large area of the deep ocean. Therefore, it is necessary to know whether the location of a sediment trap and the sampling time affect the measurements.

The deep collection of particles exhibits significant spatial heterogeneity in terms of travel time anomaly and horizontal displacement at their final positions at 1,000 m. A typical example is shown in Figures 1c and 1d to illustrate the different origins (in time and space) of the particles collected on a given day. Particles collected a few kilometers apart can have differences in travel time anomaly of up to 4 days and differences in horizontal displacement of up to 200 km. These differences, visible as strong spatial gradients in Figures 1c and 1d, appear to be associated with mesoscale and frontal structures at 200 m where the particles were seeded (Figures 1e and 1f). Furthermore, in this case, particles with shorter travel times are associated with the elongated region distant from the PAP site, while those with longer travel times are often associated with the presence of eddies. Such heterogeneity in particle collection can therefore affect sediment trap sampling and its interpretation.

The heterogeneity is, of course, strongly influenced by the sampling timescales. In Figure 2 we compare maps of particle distribution, travel time, horizontal displacement, and trajectory length binned in 10×10 km grids in the target zone over different time periods. The spatial gradients associated with these patterns, computed as differences between the values of these parameters binned in a 10×10 km grid, are shown in Figure S1 in Supporting Information S1. The patterns of particle collection and their gradients show significant hotspots and strong variations in particle parameters on weekly, monthly, and even seasonal time scales, while the patterns become more homogeneous on annual time scales and longer time scales. The example shown in Figure 2 and Figure S1 in Supporting Information S1, highlights the presence of an anticyclonic eddy that persisted around the PAP site during December 2002. The imprint of the eddy, as shown by the horizontal displacement and trajectory length in weekly and monthly averages, leads to distinct sampling areas within the collection zone. In this scenario, it is possible to sample particles from two different source areas within a small region due to the large gradients in these parameters.

To quantify these changes with sampling timescales and the generality of the patterns shown in Figures 1c, 1d, and 2, we plot the distributions of the spatial gradients for the normalized particle distribution, travel time anomaly, horizontal displacement and trajectory length for different sampling timescales over the entire simulation in Figure 3. The distributions at weekly timescales over the simulation are consistent with the previous example, leading to potentially high gradients at 10 km scale. The largest gradients can be quantified by the 90th percentile of the distribution. For the distribution of the density gradients the 90th percentile goes from values of 18% at weekly timescales down to about 8%, 5%, and 3% at monthly, seasonal and annual timescales. Similarly, for travel time, the 90th percentile goes from 0.7 days at weekly timescales to 0.12 days at annual timescales, and for horizontal displacement and trajectory length it goes from more than 50 km at weekly timescales to around 10 km at annual timescales. The time series for the spatial standard deviation derived from the gradient over the weekly time scale (Figure 4d) confirms that the standard deviation remains quite high throughout the simulation. The standard deviation for the normalized particle distribution is between 0.04 and 0.1 over the whole period, showing that the case shown in Figure 2 ($\sigma_{\nabla_{10km,N}} = 0.05$) is actually in the lower part of the variability range. The same is true for the other three parameters, highlighting that in most cases the gradients are larger than in the case shown in Figure 2 and the deep-ocean particle collection is more heterogenous. The difference between spatial gradients at seasonal and monthly scales are not that large, which suggests the persistence of the spatial heterogeneity at mesoscale lasting for several months. The result shows that particle collection measurements can be biased by the location of the traps and the sampling period on seasonal and shorter time scales. Mesoscale eddies,

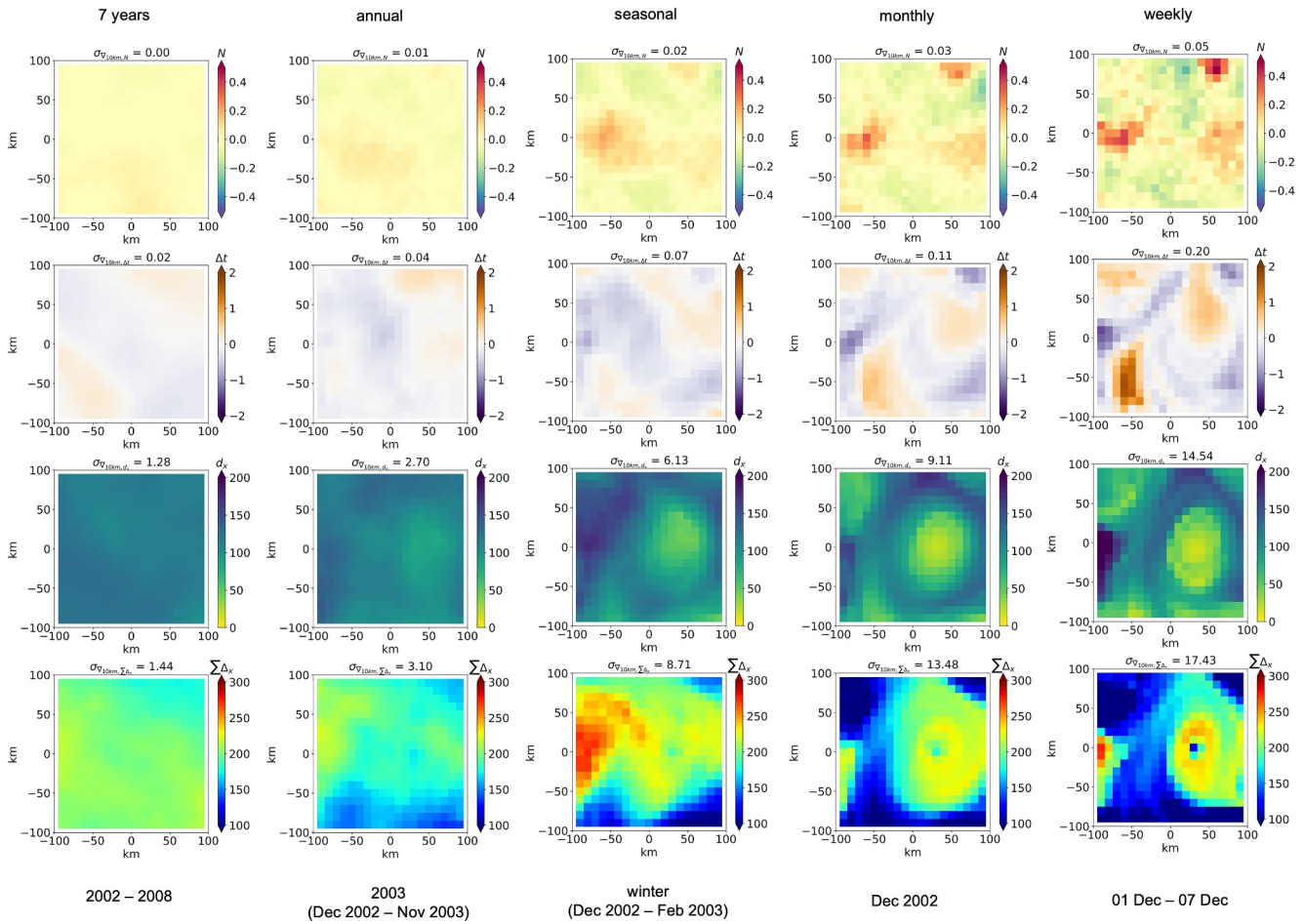


Figure 2. Particle collection in the target zone over different lengths of periods. From top to bottom: Normalized particle distribution ($N = (n - \mu)/\mu$, particle amount n in each grid cell subtracting the spatial mean μ and then divided by the spatial mean μ), travel time anomaly Δt (in days), horizontal displacement Δx (in km), and trajectory length $\sum \Delta x$ (in km) binned in 10×10 km grids on the final location of particles in the target zone for different time scales (from left to right). The standard deviation of spatial gradients is shown on top of each plot. The annual, seasonal, monthly and weekly plots are for a specific year, season, month and week.

which can persist for months in the upper ocean, significantly influence the spatial distribution of particles reaching the deep ocean.

The temporal variability of the deep-ocean particle collection is assessed by the monthly evolution of the histograms of the travel time anomaly, horizontal displacement and trajectory length, and by computing the standard deviations of their spatial gradients on the coarse-grained fields at the 10-km scale (Figures 4a–4d). Large variations and asymmetries in the travel time anomaly distribution often occur in winter and spring months when the EKE and the vertical velocities of the flow field are intensified (Figures 4e and 4f). The horizontal displacement and trajectory length show similar variability, with a high proportion of large values during the high EKE periods, in winter and spring, especially when the EKE reaches very deep. Meanwhile, the spatial gradients of the different parameters also show a significant temporal variability (Figure 4d), with the standard deviation on a weekly time scale showing a seasonality largely consistent with the seasonal variations of the EKE and vertical velocities, and an interannual variability consistent with the interannual EKE levels. There are, however, a few exceptions, in particular for the horizontal displacement and the trajectory length, where the correlation with the EKE or the vertical velocities is not so obvious for variations on timescales of a few months in low EKE periods (see, e.g., 2002). But, overall, the peaks and increasing trends of the spatial heterogeneity metrics are mostly associated with high EKE and large vertical velocities. This suggests that the large heterogeneity at depth may be connected to upper ocean signatures of eddies and fronts that are active during these months.

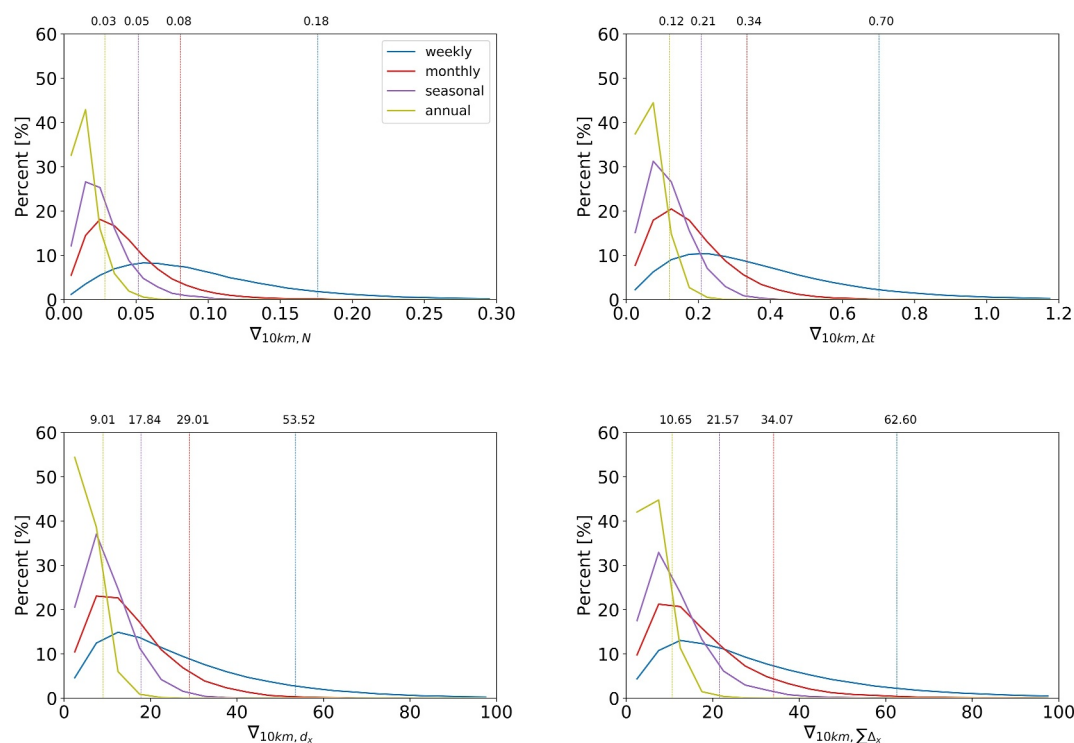


Figure 3. Distribution of spatial gradients of normalized particle distribution ($\nabla_{10km,N}$), particle travel time anomaly ($\nabla_{10km,\Delta t}$, in days), horizontal displacement (∇_{10km,d_x} , in km), and trajectory length ($\nabla_{10km,\sum \Delta x}$, in km) in Figure 2, computed as differences on a 10-km grid over different time scales. The 90th percentiles are marked as vertical dashed lines with numbers on top of each line.

Our goal now is to link the deep-sea distribution of particle trajectory properties to ocean dynamical structures. Such a link is suggested by Figures 1c–1f, but there is no simple relationship between the presence of eddies/fronts and particle trajectory. A first attempt to interpret the influence of mesoscale structures was made in Wang et al. (2022), using backtracking Lagrangian experiments from a synthetic trap at depth. The main conclusions were twofold. First, mesoscale eddies can confine particles to a more localized region, resulting in smaller horizontal displacements for particles trapped in mesoscale eddy cores. Second, particles within anticyclones tend to accelerate downward, whereas particles within cyclones generally decelerate, resulting in negative travel time anomalies in anticyclones and positive anomalies in cyclones. The trapping effect of mesoscale eddies is clearly visible for the anticyclone shown in Figure 2. However, the relationship between the presence of cyclones/anticyclones and the travel time anomaly is less obvious here, and not visible in the examples shown in Figures 1 and 2.

Specific dynamical structures in the flow field can be characterized using a vorticity-strain Joint Probability Density Function (JPDF) (Balwada et al., 2021; Shcherbina et al., 2013). The vorticity-strain JPDF decomposes the flow field into three regions based on the vertical component of vorticity and the magnitude of strain. Previously, this method was employed by Wang et al. (2022) to classify the influence of anticyclones (AVD), cyclones (CVD), and strain-dominated frontal regions (SD) on particle trajectories. Figure 5a shows such a JPDF for all particles reaching the target zone at 1,000 m, accompanied by a snapshot of the relative vorticity field highlighting the three types of flow structures (Figure 5b).

By repeating the same type of analysis with forward tracking experiments and a much larger number of particles, we obtained slightly different results compared to Wang et al. (2022). The trapping effect of mesoscale eddies is still visible, as the particles in the AVD and CVD regions have smaller horizontal displacements than those initialized in the SD regions (Figure 5d). However, a striking difference is that the travel time anomaly conditioned on the vorticity-strain space suggests a deceleration of particles in the anticyclonic structures and an acceleration of particles associated with cyclonic structures (Figure 5c), contrary to the conclusion of Wang et al. (2022).

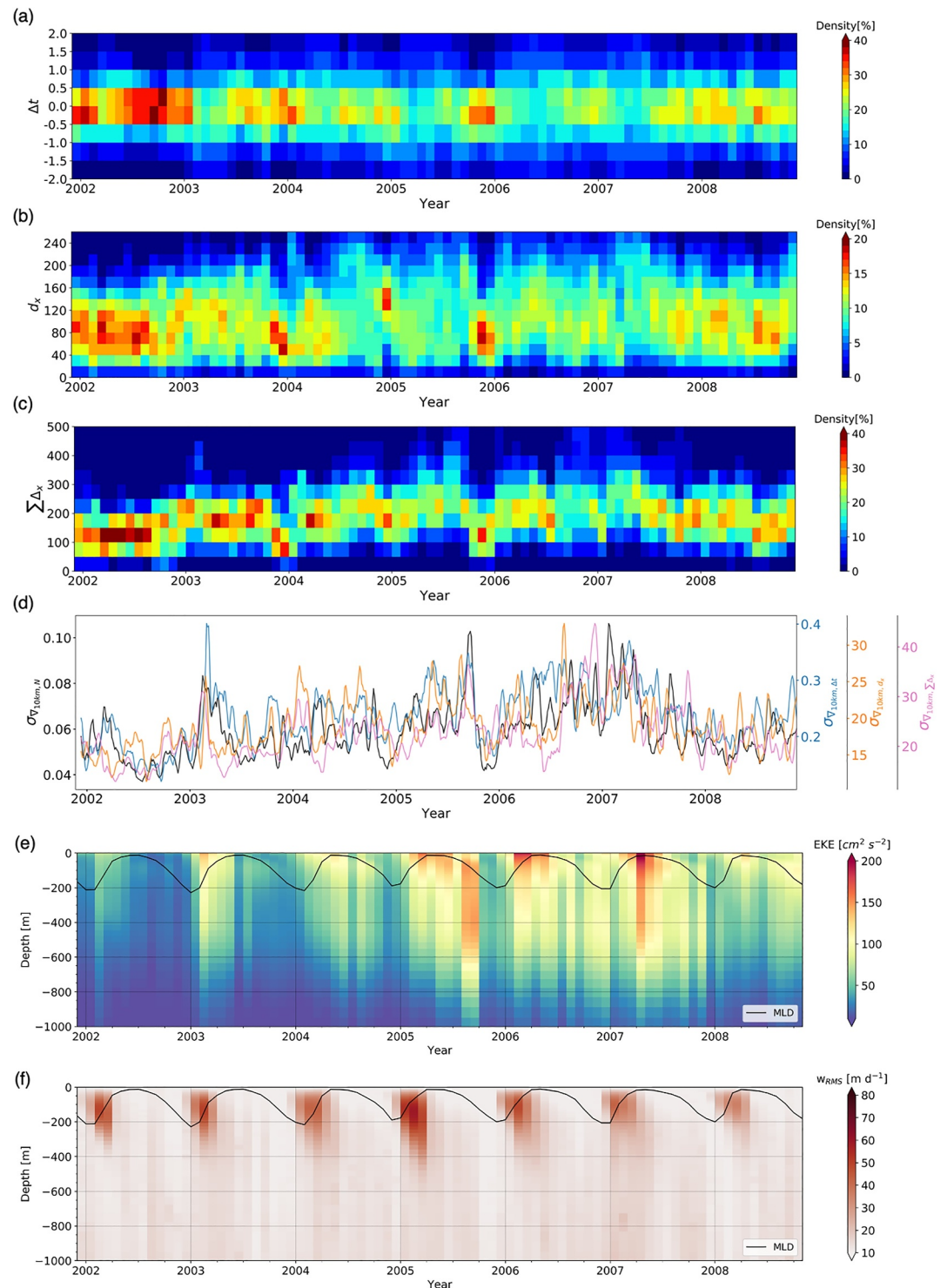


Figure 4. (a–c) Histograms of travel time anomaly (Δt , in days), horizontal displacement (d_x , in km) and trajectory length ($\sum \Delta x$, in km) varying by month. (d) Time series of spatial standard deviation derived from gradients of normalized particle distribution (σ_N), particle travel time anomaly ($\sigma_{\Delta t}$), horizontal displacement (σ_{d_x}) and trajectory length ($\sigma_{\sum \Delta x}$) computed based on 10-km horizontal grid over weekly time scale, smoothed with a monthly moving average. (e) Time series of Eddy kinetic energy (EKE) and (f) the root-mean-square vertical velocity w_{RMS} , spatially averaged over 200×200 km domain. The black curve indicates the Mixed Layer Depth (MLD).

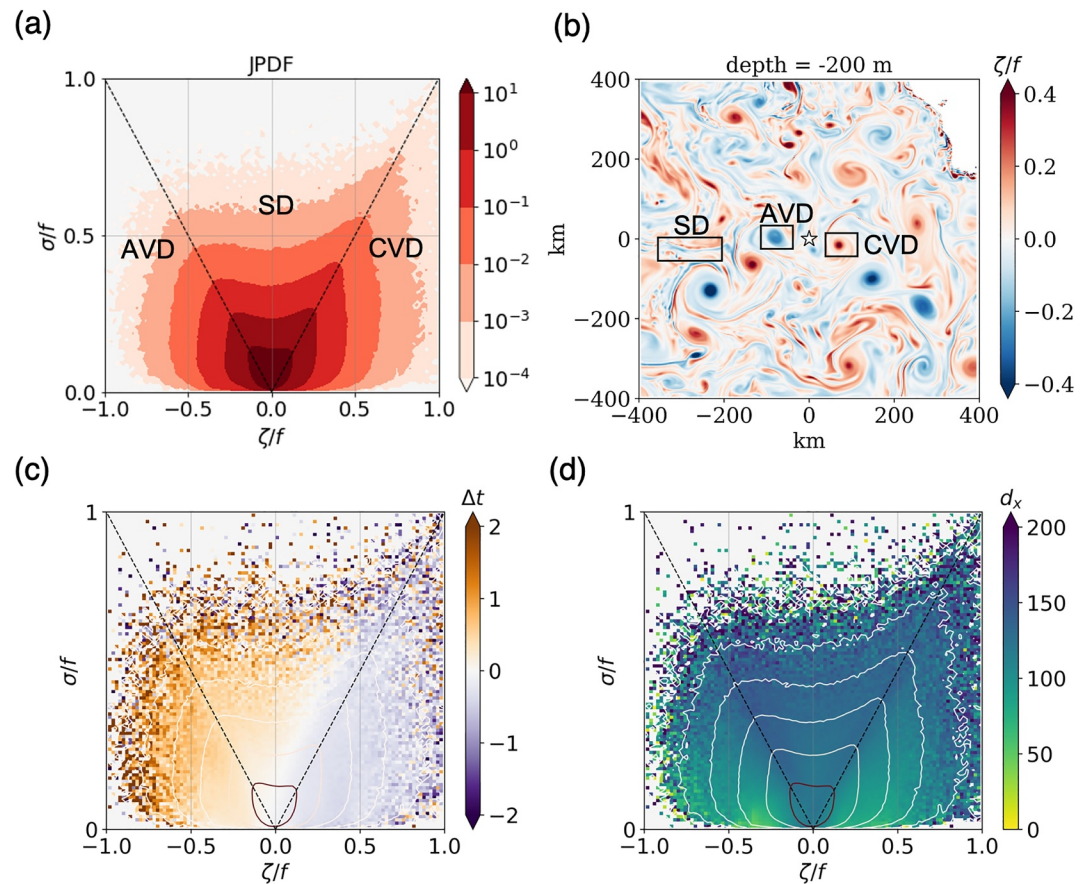


Figure 5. (a) Joint Probability Density Function (JPDF) of vorticity and strain which decomposes the flow field into regions with different dynamical features, for the initial positions (at 200 m) of all particles reaching the target zone at 1,000 m. By computing the vertical component of vorticity ($\zeta = v_x - u_y$) and the magnitude of strain ($\sigma = \sqrt{(u_x - v_y)^2 + (v_x + u_y)^2}$), the joint PDF identify three regions separated by the lines of $\sigma = |\zeta|$: SD—strain dominated $\sigma > |\zeta|$; AVD—anticyclonic vorticity dominated $\sigma < |\zeta|$ and $\zeta < 0$; CVD—cyclonic vorticity dominated $\sigma < |\zeta|$ and $\zeta > 0$. (b) An example of the relative vorticity field at 200 m showing different flow structures. (c) Travel time anomaly and (d) horizontal displacement conditioned on the 200 m vorticity-strain space.

This approach, however, has limitations, suggesting that a classification based solely on vorticity and strain may be overly simplistic. To delve deeper, the next section employs clustering analysis on the particle trajectory data to uncover more nuanced relationships between the main patterns of deep-ocean particle distributions and hydrodynamic properties.

3. Clustering Analysis

We hypothesize that the collection of particles in the deep ocean is linked to the upper-ocean flow structures where particles originate. To test this hypothesis, we perform a clustering analysis on a large data set of particle trajectories covering a broad flow field and a long time period.

3.1. K-Means Clustering

Machine learning methods have been used to map marine ecosystems (Sayre et al., 2017) and assess hydrographic regimes (Bernard et al., 2022; Hisaki, 2013; Sun et al., 2021), based on environmental metrics and ocean current data from in situ observations, satellite data, and ocean model output. K-means is a distance-based unsupervised machine learning algorithm in which data points that are close to each other are grouped into a given number (k) of clusters. Here, the input data for K-means clustering include 11 variables: the three basic particle trajectory parameters (horizontal displacement, length of particle trajectory, and travel time anomaly) and four dynamical

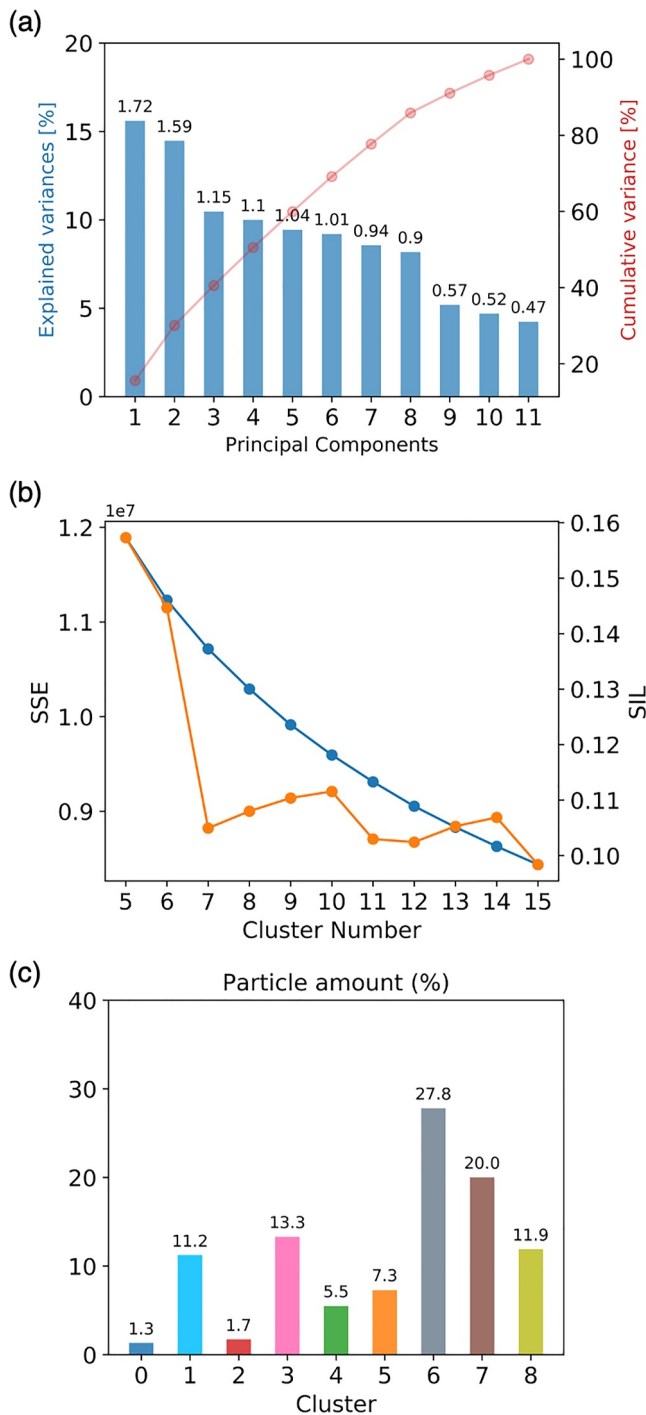


Figure 6. (a) Principle Component Analysis (PCA): Variance explained by each PC (blue: Individual, red: Cumulative), the number on top of the bars are eigenvalues. (b) Two metrics evaluate the total variation within-clusters: The sum of Squared Errors (SSE, blue curve) and the average silhouette coefficient (SIL, orange curve), against the number of clusters k . (c) The percentage of particle amount in each cluster ($k = 9$).

quantities computed from the flow field at two different depths: Okubo-Weiss parameter (OW), relative vorticity, strain, and divergence. For the two depths, we choose the seeding depth (200 m), where the initial state of the particles is determined, and the depth of 500 m, which is a transition depth for different dynamical regimes as shown in Wang et al. (2022), so that particle clusters with similar source regions and paths can be identified. We applied two data preprocessing techniques to the input data for K-means clustering.

The first is data scaling, since the attributes must have the same scale for the machine learning algorithm to consider them all as equal. Here, we used a standard scaler by removing the mean and scaling to unit variance to transform all the input variables within the range $[-1, 1]$. Principal Component Analysis (PCA) (Jolliffe, 2002) was then applied to the scaled input data to reduce dimensions and eliminate correlations. The principal components (PC) in PCA are the linear transformations of the original variables. We examined 11 PCs (Figure 6a), the same number as the input variables. Only those PCs that explain most of the variance in the data can be retained. Following Kaiser's criterion (Kaiser, 1960) that all components with eigenvalues greater than 1 should be retained, we retained 6 PCs that explained more variance than any single variable. To explain a higher total variance, we finally retained 8 PCs for the following clustering analysis, as there is a steep jump from the 8th to the 9th PC in terms of explained variance. In total, they explain about 85% of the variance, with each PC accounting for more than 5% of the variance.

The idea of defining the number of clusters (k) is to minimize the total variation (or error) within clusters. Here, we use the Silhouette Method in combination with the Elbow Method to assess an appropriate value of k for K-means (see Supplementary material for details). Figure 6b shows the curves of SSE and SIL versus k . We start with $k = 5$ to include basic groups of particles associated with specific components of the flow field: anticyclonic eddy, cyclonic eddy, fronts on both sides, and the background flow. Unfortunately, there is no obvious elbow for SSE. The highest SIL is at $k = 2$, but with a very large SSE. At $k = 10$ the SSE is much lower, collocating with a local peak of SIL. We assume that the optimal number of clusters is around 10.

The choice of k depends not only on the metric evaluation, but also on the interpretation of the clusters as representative of the underlying physical processes that transport the particles. We therefore performed sensitivity tests to validate the choice of k . The number of meaningful clusters started at $k = 5$ and increased up to $k = 10$. K-means clustering at $k = 10$ produces only a subdivision of one cluster compared to the test with 9 clusters. Therefore, the optimal number of clusters for our data is chosen to be 9. Figure 6c shows the percentage of particles in each cluster. Next, we will characterize these clusters based on the input variables for K-means clustering and present each cluster with examples.

3.2. Identification of the Clusters

The distribution of input variables in each particle cluster shows different characteristics in terms of trajectory and physical quantities (Figure 7), which are further used to define particle cluster types and names (summarized in Table 1).

We identify the first 6 clusters based on the physical quantities at 200 and 500 m, which reflect the flow structures with which the particle clusters were associated (Figures 7e–7h). Clusters 0 and 2 have distinct negative OW at both depths. According to their relative vorticity, they are classified as anticyclonic vortices (V_{AV}) and cyclonic vortices (V_{CV}), respectively. The

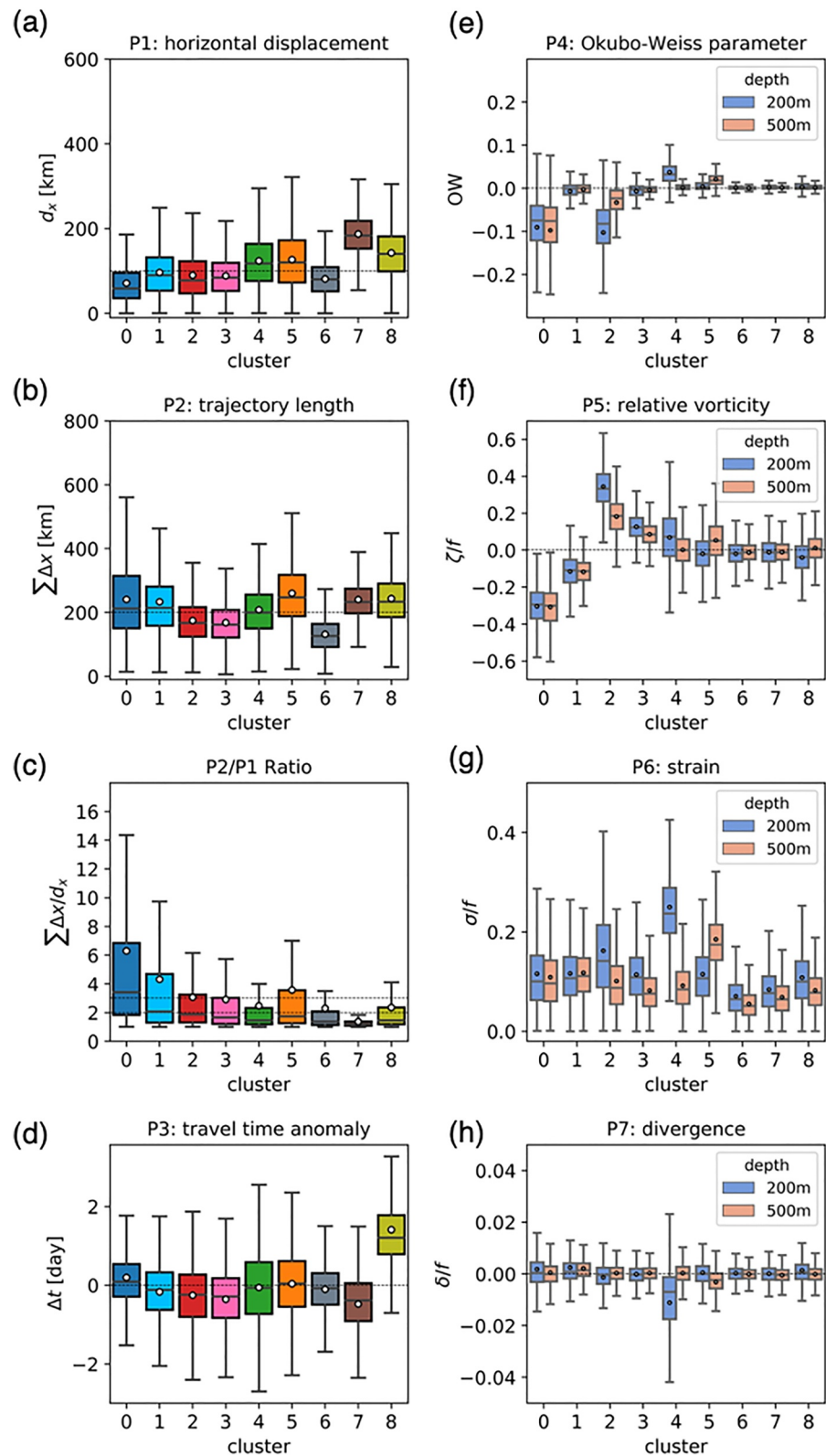


Figure 7. The distribution of variables (P1–P7 are input variables for K-means clustering, not the Ratio $\sum \Delta x/d_x$) for each cluster, showing the mean (white dots), 25%–75% interquartile range (box), minimum and maximum (horizontal bars). (a–d) Particle trajectory quantities. (e–h) Physical quantities at 200 and 500 m depth.

Table 1
Descriptive Summary of the Nine Clusters With Their Distinguishing Characteristics Shown in the Boxplots of Variables

Cluster	Characteristics	Type	Name
0	Strongly negative OW, large negative vorticity Very small horizontal displacement, very large ratio of trajectory length to displacement	Vortical, Anticyclonic Vortices	V_{AV}
1	Slightly negative OW, negative vorticity. Large ratio of trajectory length to displacement.	Vortical, Anticyclonic Spirals	V_{AS}
2	Strongly negative OW, positive vorticity. Small horizontal displacement, trajectory length several times of displacement.	Vortical, Cyclonic Vortices	V_{CV}
3	Slightly negative OW, positive vorticity. Small horizontal displacement, trajectory length several times of displacement.	Vortical, Cyclonic Spirals	V_{CS}
4	Positive OW, large strain and large negative divergence at 200 m. Large horizontal displacement, trajectory length several times of displacement.	Frontal, intensified at 200 m	F_{200}
5	Positive OW, large strain and large negative divergence at 500 m. Large horizontal displacement, large ratio of trajectory length to displacement.	Frontal, intensified at 500 m	F_{500}
6	Common physical parameters (small OW). Very small horizontal displacement, trajectory length several times of displacement.	Local sources, almost 1D vertical	$L_{Vertical}$
7	Common physical parameters (small OW). Very large horizontal displacement, trajectory length comparable to displacement, strongly negative travel time anomaly.	Remote sources, fast-moving in the horizontal, encountering more downward vertical velocity in the vertical	$R_{Fast-dw}$
8	Common physical parameters (small OW). Large horizontal displacement, trajectory length several times of displacement, distinct positive travel time anomaly.	Remote sources, fast-moving in the horizontal, encountering more upward vertical velocity in the vertical	$R_{Fast-up}$

Note. Cluster type and name are defined based on the distribution of variables in Figure 7 and Figures S1–S3 in Supporting Information S1.

structure of anticyclonic vortices is more stable when extending to deeper depths, as the change in OW and relative vorticity from 200 to 500 m is smaller for cluster 0 than for cluster 2. Clusters 1 and 3 also show large relative vorticity, but the OW values are only slightly negative. These two clusters are related to the spiral structure of the anticyclonic (V_{AS}) and cyclonic (V_{CS}) eddies, as indicated by their distribution lying around $\sigma = |\zeta|$ lines in the vorticity-strain JPDFs (Figures S2–S3 in Supporting Information S1). Clusters 4 and 5 are characterized by positive OW, very large strain and large negative divergence at 200 and 500 m, respectively. Based on their distribution concentrated in the SD region of JPDFs in Figures S2–S3 in Supporting Information S1, we inferred that particles in these two clusters are associated with frontal structures developing at the surface ocean (F_{200}) and at deeper depths (F_{500}). Note that the clusters defined here are based on the general distribution of physical quantities at 200 and 500 m, which means particles in each cluster are not strictly associated with corresponding structures concerning the dispersion of distribution shown in Figure 7. To clarify the proportion of particles in each cluster that are actually in a region of the flow that can be identified as a front or an eddy, Figure S12 in Supporting Information S1 shows the percentage of particles in each region of the vorticity-strain diagram for each cluster at 200 m. More precisely, we use the criterion $|\zeta|/f > 0.1$ to define eddy/frontal regions and $OW > 0$ to further distinguish eddies (vorticity-dominated areas) from fronts. This results in five areas in the diagram, corresponding to cyclonic fronts, anticyclonic fronts, cyclonic eddies, anticyclonic eddies, as well as the residual area. We can see that the area with the largest number of particles in each cluster is consistent with our initial identification of the clusters, even if this criterion for identifying fronts and eddies is rather simplistic and debatable.

The four clusters associated with eddy structures (V_{AV} , V_{CV} , V_{AS} , V_{CS}) have small horizontal displacements with a median and mean of less than 100 km, especially cluster V_{AV} associated with anticyclonic vortices, where about 75% of the particles originate close to the collection point ($d_x < 100$ km). As expected, the trajectory length of particles in these vortical clusters is much larger than the horizontal displacement (mean ratio $\sum \Delta x/d_x$ above 3), implying that particles are swirling in these structures. Interestingly, the anticyclonic vortical structures appear to have stronger trapping effects on sinking particles than their cyclonic counterparts, as indicated by the particle trajectory length, which show larger values for clusters V_{AV} and V_{AS} than for clusters V_{CV} and V_{CS} (Figure 7b). In particular, the trajectory length is on average 6 times the horizontal displacement for particles in anticyclonic vortices (V_{AV}). The travel time anomaly for V_{AV} is also larger, with more positive values than the other three vortical clusters (Figure 7d), which means that the collection of particles at depth is often delayed by the vertical flows. On the contrary, anticyclonic spirals and cyclonic vortices/spirals tend to accelerate the sinking of particles. Particles in the core of anticyclonic vortices are more likely to be slowed down, as opposed to particles in the anticyclonic spirals, which are more likely to be accelerated. The two clusters associated with frontal regions show larger horizontal displacements than the vortical clusters, along with large trajectory lengths comparable to the horizontal displacements (moderate ratio). Indeed, the frontal structures transport particles far from the source compared to the more local mesoscale eddies.

The last three clusters exhibit common distributions of physical quantities, with less prominent features than the first six clusters. Relying solely on physical parameters is insufficient to distinguish these three clusters; thus, trajectory parameters (Figures 7a–7d) are employed for this purpose. These clusters collectively account for over 50% of the total particles (Figure 6d). Cluster 6 is the largest, comprising 27.8% of the particles (Figure 6d). It has the smallest source region for particle initialization (Figure S4 in Supporting Information S1), with the smallest horizontal displacement and trajectory length among all clusters. As it is much less affected by horizontal advection, we label it “ $L_{Vertical}$.” This cluster is also situated in regions with weak vertical currents, as indicated by the smallest range of travel time anomalies. Namely, it is associated with the local background flow, suggesting a calm ocean environment. Clusters 7 and 8 exhibit the largest and second-largest displacements, respectively, but with contrasting travel time anomaly distributions (most negative vs. most positive). The rapid particle motion in these clusters could be driven by strong horizontal velocities in the veins and filaments of the flow field. The inverse distribution of travel time anomalies in these two clusters is attributed to different vertical flows encountered during sinking (more downward or upward vertical velocities). We define these clusters as fast-moving particles from distant source regions, associated with downward ($R_{Fast-dw}$) and upward ($R_{Fast-uw}$) vertical velocities in the flow field.

Finally, for the nine clusters, we evaluate the vertical distributions of along-trajectory relative vorticity, Okubo-Weiss parameter (OW), instantaneous horizontal displacement and vertical displacement anomaly between 200

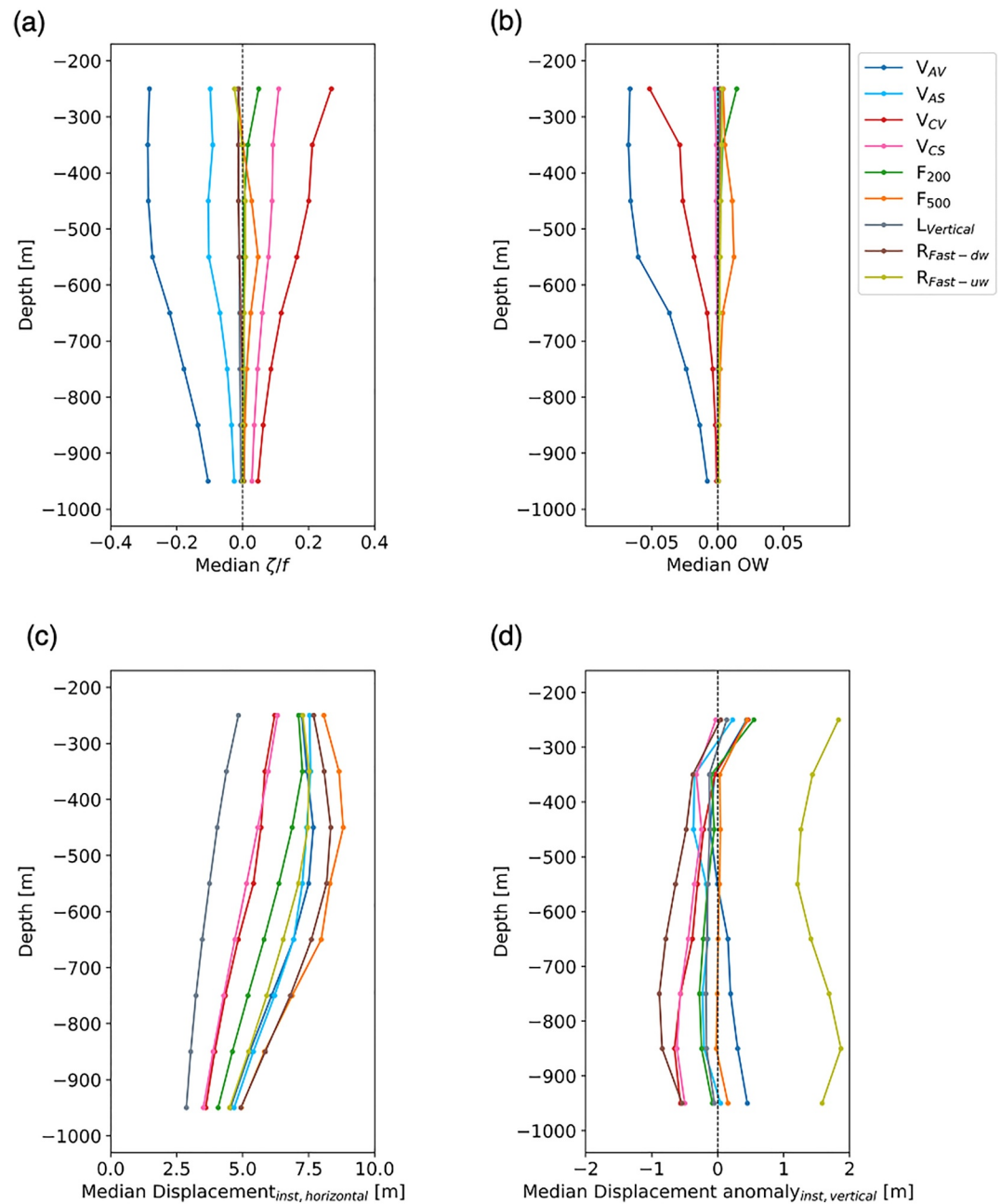


Figure 8. Medians of panel (a) relative vorticity, (b) Okubo-Weiss parameter, (c)–(d) instantaneous horizontal and vertical displacement (anomaly) along particle trajectory in different depth ranges. The vertical displacement anomaly is the difference between particle depth and its expected depth without impacts of vertical flows, with negative (positive) values corresponding to faster (slower) sinking.

and 1,000 m. Figure 8 shows the median of the four variables at each depth level (the full distributions are available in Figures S5–S8 in Supporting Information S1). Overall, the vertical distributions of relative vorticity and Okubo-Weiss parameter for the clusters (Figures 8a and 8b) are consistent with their characteristics at 200 and 500 m (Figures 7e and 7f). Particles in clusters V_{AV} and V_{CV} are mostly associated with the mesoscale anticyclonic and cyclonic vortices throughout the water column, as indicated by the negative Okubo-Weiss parameter and negative/positive relative vorticity. The full vertical structure confirms that the anticyclonic vortices are more coherent than the cyclonic vortices at each depth level, especially below 600 m where the signals from the cyclonic vortices weaken. Although the spiral clusters (V_{AS} and V_{CS}) differ from the vortical clusters (V_{AV} and

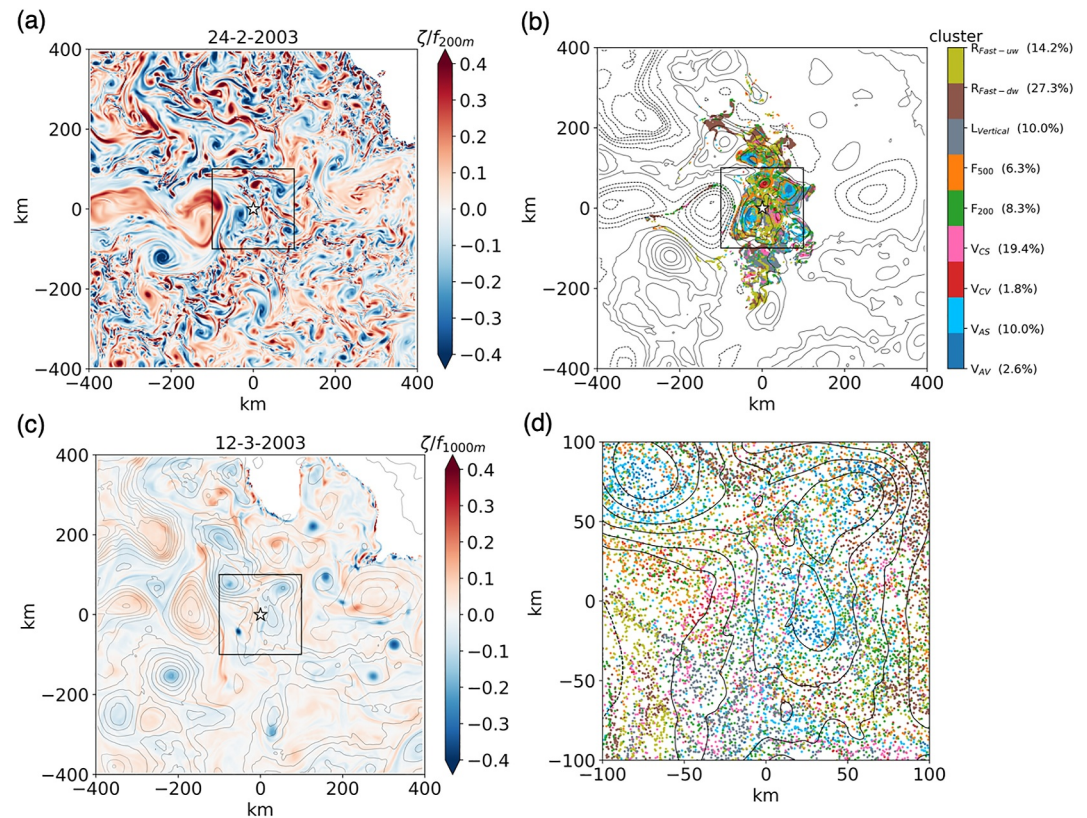


Figure 9. Clusters identified for particles released on 1 February 2003 reaching the 200×200 km target zone. (a) The relative vorticity field at 200 m. (b) The initial positions of particles at 200 m are colored by the clustering results, with Sea Surface Height (SSH) contours flow structures (solid lines for anticyclones and dashed lines for cyclones). (c) The relative vorticity field at 1,000 m with SSH contours after 16 days (idealized reaching time of particles). (d) The final position of particles in the target zone (the reaching time may depart from the date on the left), with SSH contours at the idealized reaching time.

V_{CV}) in terms of physical quantities, they have similar characteristics for the horizontal transport of particles (Figures S7 in Supporting Information S1). The vertical transport of particles in the vortical and spiral clusters is more difficult to interpret. On average, particles in clusters V_{AS} , V_{CV} and V_{CS} tend to sink faster than those in cluster V_{AV} , despite depth-dependent variations.

The frontal cluster F_{200} shows an asymmetry toward positive OW and positive relative vorticity from 200 to 400 m (intensified at 200 m), while F_{500} shows such a feature from 400 to 800 m (intensified at 500 m). The instantaneous horizontal displacement of particles in clusters $R_{Fast-dw}$ and $R_{Fast-uw}$ show similar profiles of medians with peaks at about 500 m depth. Their difference in instantaneous vertical displacement is much more pronounced than in the horizontal. Particles in cluster $R_{Fast-dw}$ experience upward vertical velocities below 300 m, which increase until 700–800 m. Meanwhile, particles in cluster $R_{Fast-uw}$ are initially largely decelerated. The deceleration diminishes until 500 m but intensifies again to a peak at 800–900 m. The profiles suggest that currents below 500 m, not necessarily associated with a strong vorticity signature at 200 or 500 m, play an important role in controlling the vertical sinking of particles in these two clusters.

3.3. Typical Clusters Examples and Spatial Variability at Depth

Here we show clustering results for particles released on three different days to visualize the identified clusters and to establish the link between the spatial variability of the particle collection at depth and the surface signatures. The relative vorticity field at 200 m shows three examples characterized by different features. The first case, taken in the winter 2003, shows rich small-scale structures with embedded submesoscale vortices (Figure 9a). The main structure around the PAP site consists of three anticyclones and a chain of smaller cyclonic

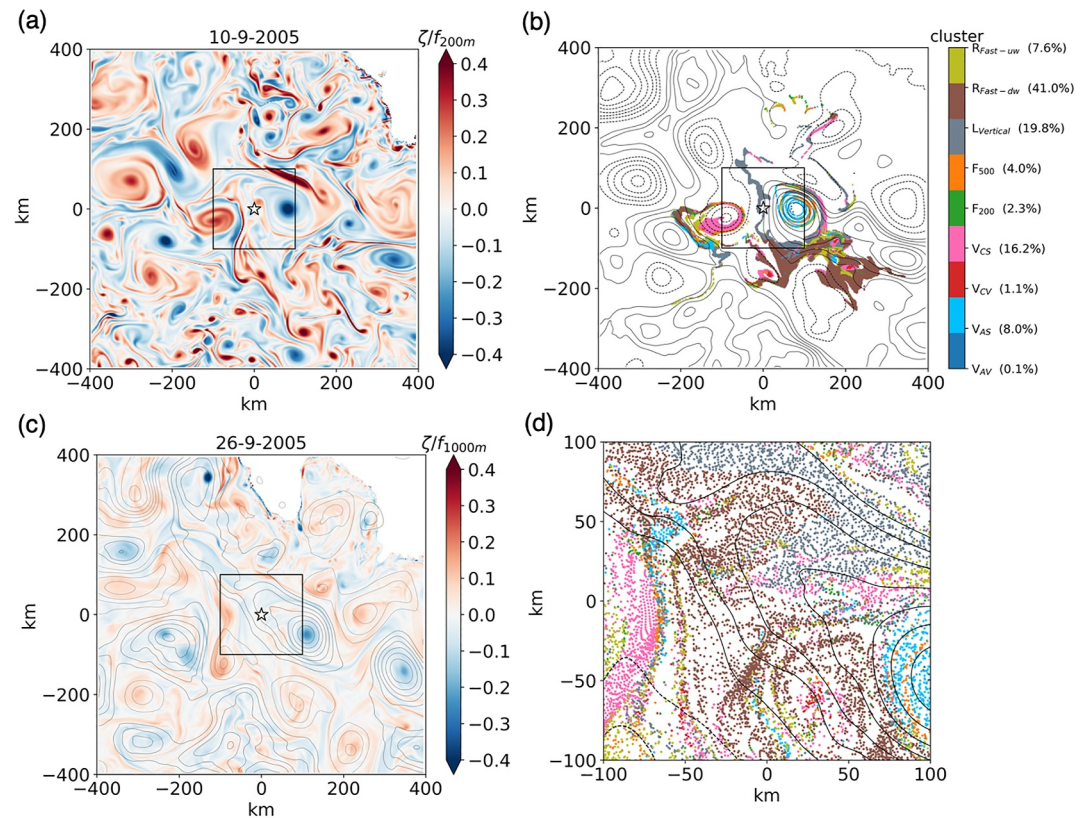


Figure 10. Same as in Figure 9, but for particles released on 10 September 2005 reaching the target zone.

vortices. The second case, from autumn 2005, has a dipole located above the PAP site (Figure 10a). The flow field has much fewer small-scale structures than in the winter case, but more large mesoscale eddies. The third case, from spring 2007, is in an intermediate state with both mesoscale eddies and small-scale filaments and vortices (Figure 11a). An anticyclonic mesoscale eddy is situated at the PAP site.

The particle sources in the first case display a more homogeneous distribution of clusters compared to the other two cases (Figures 9–11b, the distribution of each cluster is available in Figures S9–S11 in Supporting Information S1). Across all three cases, the K-means clustering approach successfully identifies the cores of mesoscale eddies and a set of small-scale vortices (clusters V_{AV} & V_{CV}), as well as spirals of varying sizes (clusters V_{AS} & V_{CS}). However, only a limited number of particles are clustered as V_{AV} & V_{CV}, with these clusters comprising less than 10% of the total, particularly in the autumn case. A larger proportion of particles are associated with the spiral structures, ranging from 8% to 20%. The distributions of clusters V_{AS} and V_{CS} indicate particle transport by spirals as they move horizontally. In the first case, cluster F₂₀₀ is the second largest, containing 16.7% of the particles. Since surface-intensified fronts are predominantly generated in winter and spring (Taylor & Ferrari, 2011; Yu, Naveira Garabato, Martin, Gwyn Evans, & Su, 2019), the two frontal clusters account for 26.4% of the particles initially distributed in a soup of small-scale structures surrounding the chain of eddies. In the third case, in early spring, clusters F₂₀₀ and F₅₀₀ are not as large as in the winter case, showing patchy sources within the eddy soup. Frontal structures are less active in autumn, with each cluster containing less than 5% of the particles in the second case. The last three clusters, originating from areas between the eddies, contribute about 40%–70% of the particles. Cluster L_{Vertical} is mostly concentrated above or near the edge of the target zone. The fast-moving cluster R_{Fast-dw} in the vein field is always a significant contributor, especially in the autumn case, where it accounts for 41% of the particles.

The distribution of particles in the target zone at 1,000 m still shows a clustering pattern (Figures 9–11d). This pattern is more obvious in the latter two cases, while the first case appears more scattered due to the influence of smaller structures. The relative vorticity map at 200 m on the particle release day, combined with the map at 1,000 m after 16 days, provides insight into the evolution of the flow field during particle sinking. The alignment

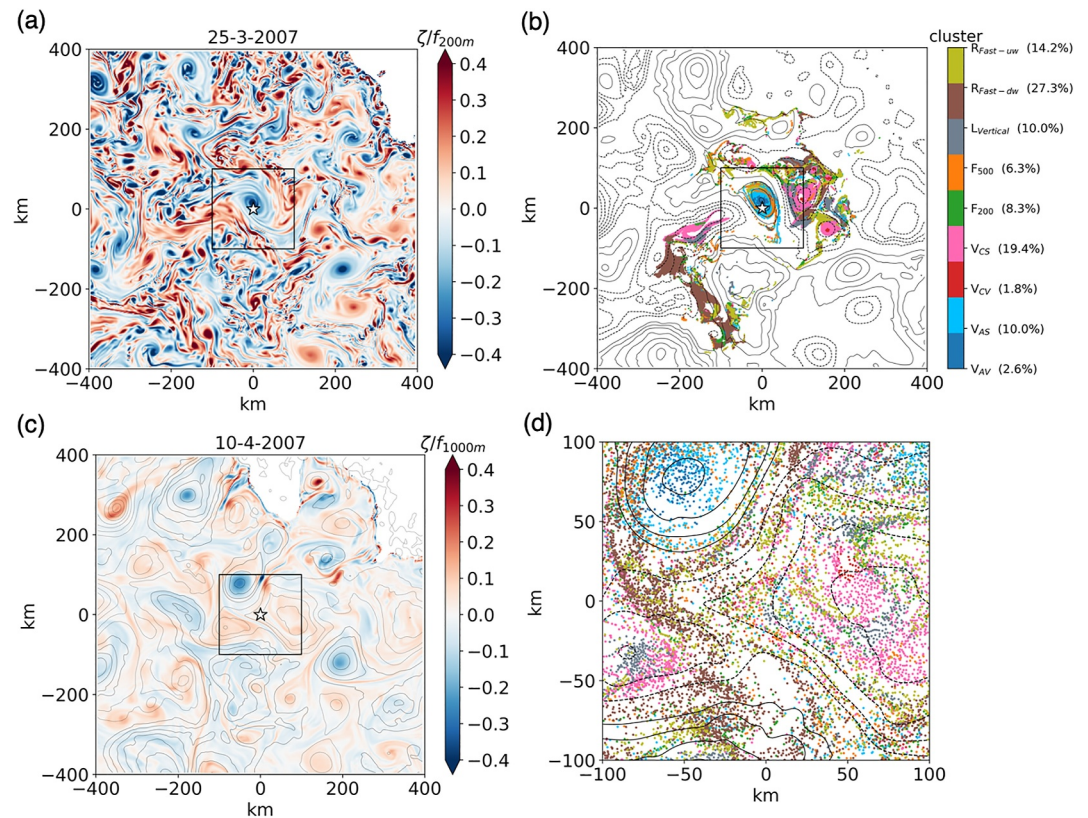


Figure 11. Same as in Figure 9, but for particles released on 25 March 2007 reaching the target zone.

of the vorticity field at 1,000 m with SSH contours indicates the presence of deep-reaching eddy structures. For example, the three anticyclones around the PAP site in the first case and the one at the site in the third case move northwards, while the dipole in the second case diverges. Particles associated with vortical and spiral structures typically follow these movements, resulting in a patchy distribution at depth that aligns with the main pattern of the dynamical structures. Notable distributions include V_{CS} on the west edge and V_{AS} on the southeast edge in the second case, the anticyclonic imprint in the northwest and V_{CS} in the east of the third case. The spatial organization of particle clusters in the target zone shows that the heterogeneity of deep-ocean particle collection can be linked to surface signatures. This implies that sediment traps may collect particles from similar sources or entirely different sources, depending on the exact location of the trap at depth.

4. Seasonality of Deep-Ocean Particle Collections

The 7-year simulations reveal seasonality in terms of both particle clustering and heterogeneity of particle collection at depth. Although the total number of particles reaching the target zone at each time step remains around 10 thousand with slight fluctuations, particles in different clusters exhibit seasonal variability over the seven years, as well as interannual differences (Figure 12a). Clusters $L_{Vertical}$ and $R_{Fast-dw}$, which account for almost 50% of the total particles (Figure 6d), dominate most of the time, with peaks in autumn or early winter. More particles are identified in other clusters from late winter to the end of summer. To better visualize their temporal variations, the clusters are further divided into four groups shown in Figures 12b–12e.

Over the entire period, only 3% of the particles belong to the vortical clusters V_{AV} and V_{CV} (Figure 6d). These two comparable eddy-core related clusters show similar seasonal variations of particle amount in both timing and magnitude (Figure 12b). Peaks often occur in late winter or early spring, followed by a gradual decline until reaching second peaks in late summer of some years. After these summer peaks, the two clusters remain at low levels for the following months, when the last three clusters ($L_{Vertical}$, $R_{Fast-dw}$, $R_{Fast-uw}$) dominate. Less than 4% of the particles are associated with coherent vortices most of the time, despite occasional spikes up to 8%.

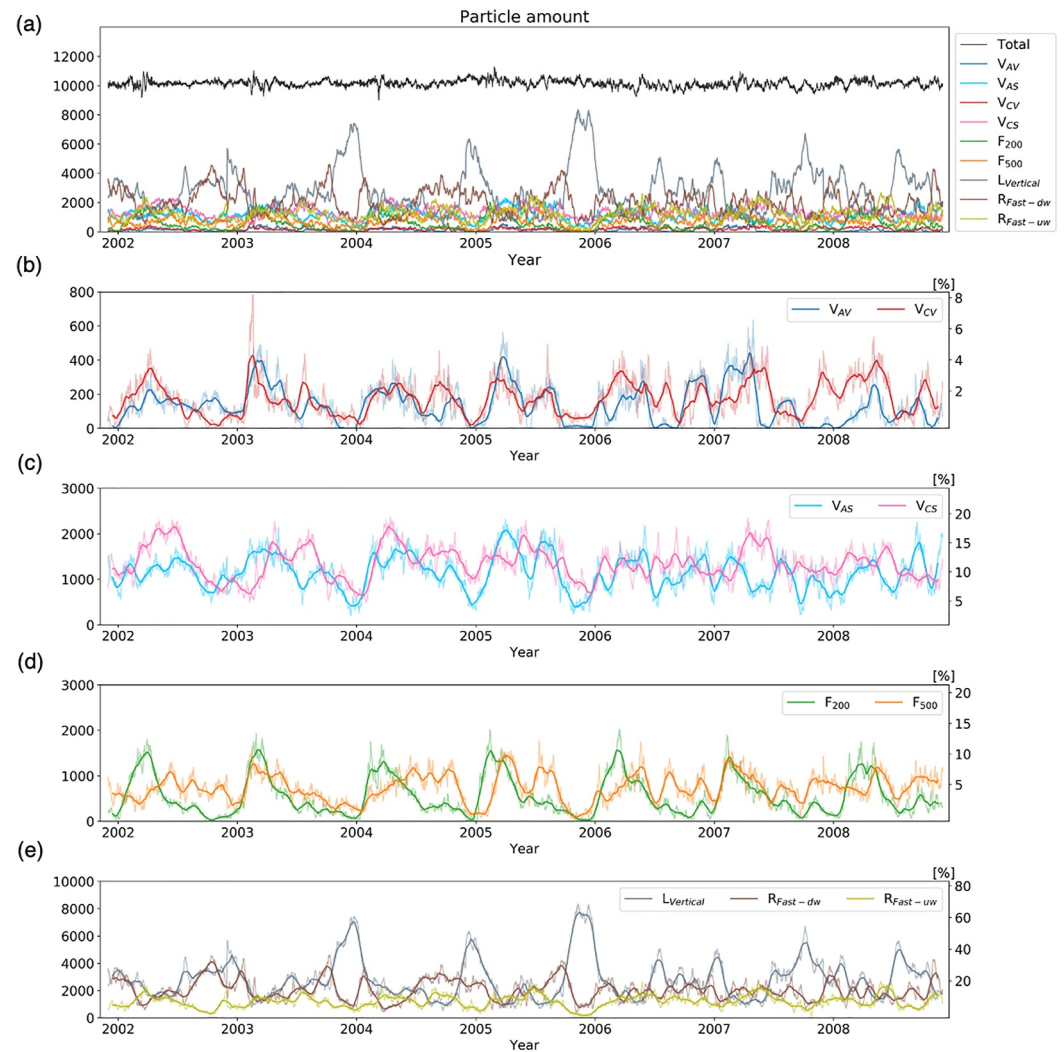


Figure 12. Time series of particle amounts in clusters. (a) At 12 hr intervals for all clusters, the total amount of particles reaching the target zone is shown as the black thin line on the top. (b)–(e) Four groups of clusters with adjusted y-axis range, the numbers on the left and the percentages on the right. The thin curves in light colors are the same as in panel (a) at 12 hr frequency, and the thick lines are 30-day moving averages based on the thin curves.

The timing of the peaks and troughs of vortical clusters V_{AS} and V_{CS} (Figure 12c) appears to mirror the variability of V_{AV} and V_{CV} . However, the spiral clusters V_{AS} and V_{CS} are more stable, fluctuating around 1,000–2,000 particles per 12-hr time step reaching the target zone. These clusters contain 3–5 times more particles than the vortical clusters, accounting for over 20% of the particles in the target zone. This indicates that the hydrodynamic characteristics of the spiral structures around mesoscale eddies in this region likely play a more significant role in particle export throughout the year, compared to the eddy cores, which are primarily active during the winter-spring period and occasionally in mid-summer. This highlights the importance of sampling the entire eddy structure rather than just the eddy core. Interestingly, V_{CS} and V_{CV} tend to have more particles than their anticyclonic counterparts (total 0.4% and 2.1%, respectively, Figure 6d). This discrepancy may be due in part to an asymmetry in the areas covered by cyclones and anticyclones at the time of particle seeding.

The frontal cluster F_{200} exhibits the most pronounced seasonality, with peaks reaching up to 15% in spring (Figure 12d). The timing of these peaks varies annually and between the two clusters (F_{200} and F_{500}). The peaks of F_{200} occur with similar magnitude each year from February to April, aligning with active frontogenesis processes in the upper ocean (Yu, Naveira Garabato, Martin, Buckingham, et al., 2019). The frontal regions are also characterized by enhanced vertical velocities extending from the sea surface down to hundreds of meters below

the mixed layer (Klein & Lapeyre, 2009; Lévy et al., 2012; Mahadevan & Tandon, 2006), as shown in Figure 4c with large variations developing from January and intensifying until March. While F_{200} is larger than F_{500} in winter-spring, it becomes much smaller in summer and autumn. The high values of F_{500} occurring in spring synchronize with the peaks of F_{200} or show a delay of one or 2 months. Peaks of F_{500} are also observed in the summer and autumn months, possibly related to the eddy activity indicated by the EKE time series (Figure 4b). For example, the peaks of F_{500} observed in summer and autumn from 2004 to 2008 correspond to the deep penetrating large EKE during these months. The cluster maps in Figures 9c and 10c show that particles clustered in F_{500} are initialized in frontal regions at the edges of eddies. Therefore, small-scale and mesoscale eddies as well as fronts are important areas to understand the properties of particle export in winter and spring, while the mesoscale eddy boundaries are most important in summer and autumn.

Overall, the last three clusters ($L_{Vertical}$, $R_{Fast-dw}$ and $R_{Fast-uw}$) contain 59.7% of the particles (Figure 12e). These clusters, which are less influenced by mesoscale dynamics, dominate in autumn. The local background flow is of leading order, while clusters $R_{Fast-dw}$ and $R_{Fast-uw}$ are potentially associated with large-scale dynamics, or small-scale dynamics (submesoscale filaments). It is interesting to note that cluster $L_{Vertical}$, with negligible effects of the dynamics in both horizontal and vertical directions, is the largest of the nine clusters we identified. Particle clustering in $L_{Vertical}$ can account for 40%–70% in November–January, which is also inferred from the histograms of horizontal displacement and trajectory length (Figures 4b and 4c). This suggests that most of the particles collected in the deep ocean are locally exported over relatively short distances by the background flow. The transport of particles from distant sources, represented by $R_{Fast-dw}$ and $R_{Fast-uw}$, shows no clear seasonality. Each of these clusters can contribute up to 20%–30% of the total particles for several months each year, warranting further investigation of mesoscale activity and large-scale dynamics.

5. Discussion and Conclusions

5.1. Impacts of Different Dynamical Structures on the Particle Collection

This study investigates the connection between deep-ocean sinking particles and surface ocean dynamics by simulating particle trajectories over 7 years in an open-ocean region centered on the PAP site in the Northeast Atlantic. Specifically, we examine particles released at a depth of 200 m, with a sinking velocity of 50 m/day that ultimately reach a 200×200 km target area at a depth of 1,000 m.

This extensive data set of forward particle trajectories enables us to explore the spatial and temporal variability of deep-ocean particle collections near the PAP-SO site. Surface variability introduces significant heterogeneity at depth, which diminishes as the sampling period extends. Over the long term, spanning a year or more, regional differences become negligible. However, in the short term, spatiotemporal variations in mesoscale activity significantly influence the spatial distribution of particle collections at depth. Particles with diverse properties form mesoscale heterogeneous patterns, clearly reflecting the impact of eddies and frontal structures. Figure 2 shows that, on a weekly and even monthly scale, the variability in particle numbers can vary by 40%–50%. Estimates of the error in sediment trap data are extremely difficult to assess. Although the potential biases affecting trap efficiency are well known (local hydrography due to trap geometry, swimmer interference, solubilization, drifting vs. fixed moorings), techniques exist to minimize or estimate these errors (Buesseler et al., 2007), with the relevant radionuclide budget consisting of a proven approach. Buesseler et al. (2007) estimates that, for shallow depths (40–150 m), ^{234}Th tends to show that under-trapping could reach a factor of two. So, even if it is smaller, the impact of small (in time and space) circulation scales on particle fluxes induces a non-negligible error, all the more so as trapping biases tend to decrease rapidly with depth (less energetic hydrodynamics, less zooplankton).

Applying K-means clustering to the particle trajectory data reveals nine distinct particle clusters, corresponding to various dynamical structures such as eddies, fronts, and background flows. By using a machine learning method on this extensive data set, we can statistically characterize the eddy field and determine the contribution of different circulation features to deep-ocean particle collection. This clustering result is also assessed by checking the proportion of particles classified in different regions in the vorticity-strain JPDF at 200 m after applying a criterion $|\zeta|/f > 0.1$ (Figures S12–S13 in Supporting Information S1). Overall, the K-means clustering method captured the particles that were initially located in the eddy and frontal regions well. However, it also includes particles that are not in eddy/frontal regions at 200 and 500 m according to our criteria. It can be inferred that the clustering is based on similarities in trajectories, which may be due to the presence of fronts and eddies at depths

other than 200 and 500 m. However, this remains something that needs to be assessed more carefully and is just a hypothesis at this stage.

While cyclonic eddies contribute slightly more particles to the target area (2.5% of the total), anticyclonic eddies demonstrate greater coherence and stronger trapping effects on sinking particles. Furthermore, eddy cores (vortices) and eddy perimeters (spirals) influence particle transport differently in terms of horizontal and vertical dynamics. More particles are associated with spiral structures than with vortices, indicating that spirals play a more significant role in particle transport than eddy cores.

In the vertical, anticyclonic spirals and cyclonic vortices/spirals generally accelerate particle sinking, while anticyclonic vortices slightly slow it down. However, these findings represent average values for each cluster, and the distributions of vertical velocity and travel time anomalies show significant variability inside each cluster. Furthermore, these results partially contradict the conclusions of Wang et al. (2022), which indicated that anticyclonic vortices tend to accelerate particle sinking, while cyclonic vortices slow it down, based on a much more limited number of events. This again highlights how sensitive these results are to the way they are diagnosed. In Wang et al. (2022), the vertical velocities were calculated at each depth and plotted as a function of vorticity and strain at the same depth. Here we return to a classification of the trajectory mean vertical velocity or time anomaly based on the vorticity and strain at the export depth, which explains the contrasting result. Overall, the dynamics driving vertical motions within mesoscale eddies are very complex and cannot be reduced to conventional models such as “eddy pumping” or “eddy-Ekman pumping,” as various processes can create patchy vertical velocity patterns. For instance, a synthetic analysis of a mesoscale cyclonic eddy revealed azimuthal wave-like patterns in the vertical velocity field, associated with vortex Rossby waves (VRWs) (Nardelli, 2013). Virtual particle trajectories within this eddy showed average upwelling in the eddy core, downwelling in the intermediate region (defined by maximum kinetic energy), and upwelling again at the eddy periphery. The variance in vertical velocity within eddies can largely be attributed to alternating upward and downward cells, influenced by changes in eddy shape over time due to perturbations in geostrophic flow (Pilo et al., 2018). Chen et al. (2020) also demonstrated that the vertical velocity field within a large anticyclonic warm core ring can evolve from dipolar to multipolar patterns under different dynamical processes over the ring's lifespan. Therefore, the effect of eddy structure on particle flux remains an open question that cannot be answered in general terms but requires detailed analysis of individual eddies.

Frontal structures play a role at the initial seeding depth of 200 m and at 500 m, near the permanent thermocline in this region (Callies et al., 2020), where deep fronts or filaments develop due to baroclinic instability. The circular shape of cluster F₅₀₀ in the examples (Figures 9–11b) and its particle amount peaks (Figure 12d) during high EKE periods suggest that vortex Rossby waves (VRWs) may be involved. These waves emerge from vortex strengthening or decaying under background deformation in an external strain field (McWilliams et al., 2003). Such vorticity filaments within mesoscale eddies are identified as biogeochemical footprints of vertical motions induced by VRWs (Z. Zhang & Qiu, 2020).

Another key finding is that particle clusters exhibit distinct seasonality related to mesoscale eddy activity and frontal development. All eddy and frontal clusters are active in winter-spring, with spirals and deep fronts also contributing significantly in summer. The spring-summer periods, dominated by vortical and frontal clusters, are associated with high EKE and large vertical velocities, leading to high spatial heterogeneity in deep-ocean particle collection (Figure 4). This highlights the importance of fronts and eddies for deep-sea particle flux during winter-spring or summer. The dominance of front and eddy-related clusters in winter and spring is largely related to the larger proportion of fronts and eddies in surface water during these periods, even if there is not a one-to-one correspondence between the clusters and the properties at 200 m (Figure S13 in Supporting Information S1).

The stirring and trapping effects of eddies (McGillicuddy, 2016) and the convergent zones at fronts (D'Asaro et al., 2018) can redistribute and concentrate particles. Previous studies have suggested enhanced particle flux at fronts and eddies due to strengthened vertical motions (Dever et al., 2021; Omand et al., 2015; Resplandy et al., 2019). While we assume homogeneous surface particle production and do not address real particle flux, further assessment is needed to consider biological or biogeochemical interactions. Increased nutrient supply at fronts and eddies can fertilize phytoplankton growth and particle production (Hosegood et al., 2017; Mahadevan & Archer, 2000). Particle size structure is also crucial, with large particles forming and accumulating rapidly at the base of the mixed layer during early bloom stages (Jouandet et al., 2014). Larger, fast-growing species like diatoms, which produce large sinking particles, are more concentrated at frontal regions and contribute to particle

flux episodes (Kemp et al., 2006). The coupling of the purely dynamic transport investigated in this study with the spatiotemporally varying intensity of primary production suggests that the role of eddies and fronts in carbon export is weak in early winter and amplified during the spring bloom period.

The simulations presented here build upon the findings of Wang et al. (2022), as their backward simulations identified only a few typical cases of eddy presence, which may not represent broader conditions. Our analysis of particle distribution within a 200×200 km target zone in the deep ocean differs from the point-like particle collection in backward simulations, which had a limited number of particle trajectories. This approach strengthens the connection between upper-ocean signatures and deep-ocean heterogeneity in particle sampling. This is illustrated by the contrasting results on the effect of cyclonic and anticyclonic eddies on time travel anomalies, based on a limited number of eddies (about four each) sampled in Wang et al. (2022). Using a large number of particles and clustering methods, we have found that the particle trajectories described in Wang et al. (2022) as typical of anticyclonic eddies are in fact more associated with the anticyclonic spirals (V_{AS}) than with the anticyclonic cores (V_{AV}). Similarly, the cyclonic eddies show a much more contrasting effect on the travel time anomalies, and the particle trajectories described in Wang et al. (2022) as typical of cyclonic eddies are in fact a combination of V_{CV} , V_{CS} and $R_{Fast-uw}$, the fraction of the latter being sufficient to affect the mean travel time anomaly.

While particle transport in the mesopelagic layer varies among clusters—with greater trapping in anticyclones and “quiet” zones (almost 30% of the total particle collection) and differing travel time anomalies, both eddy-related clusters and the background cluster are nearly one-dimensional on the cruise time scale. Comparing particle collection over different periods suggests that measurements taken over several days to several months can vary significantly depending on the sediment trap location. The strong variability in the effect of dynamics on particle capture highlights the need for clustering sediment traps to account for spatial variability. Specifically, for particles in clusters F_{200} , F_{500} , $R_{Fast-dw}$, and $R_{Fast-uw}$, a Lagrangian sampling strategy would be more efficient. This underscores the importance of deploying mooring arrays of sediment traps or autonomous moving traps in the deep ocean and comparing Lagrangian and Eulerian sampling strategies over weekly to monthly time scales.

5.2. Limitations and Future Directions

This study demonstrates that ocean dynamics can induce significant spatial variability and seasonal changes in deep-ocean particle collection, independent of biological source heterogeneity. However, the approach has several limitations that could be addressed.

Firstly, the deepest mixed layer depth in winter in our study region is around 200–300 m (Yu, Naveira Garabato, Martin, Buckingham, et al., 2019). The choice of a fixed export depth at 200 m and a constant sinking velocity of 50 m d^{-1} in this study only considers particles that rapidly transport surface production below the mixed layer. While a significant proportion of carbon flux to the deep sea occurs this way (Riley et al., 2012), particle origins and processing in the water column are more complex, with highly variable compositions and sinking speeds (Huffard et al., 2020). Observed particle sinking rates at the PAP site range from 30 m d^{-1} to 180 m d^{-1} (Riley et al., 2012; Villa-Alfageme et al., 2014). Our choice of 50 m d^{-1} is close to the lower bound of the sinking velocity range in this region. The variability of particle sinking time and locations will be reduced if larger sinking speeds are considered and if multiple sinking speeds are used simultaneously. On the other hand, the impact of physical currents on slower sinking particles (e.g., 20 m d^{-1}) will substantially increase, as illustrated by Wang et al. (2022). Furthermore, the sinking velocity in reality is not constant due to the influence of various processes such as remineralization, aggregation, fragmentation and decomposition. Therefore, our approach is certainly very simplified and could lead to an overestimate of the variability, but, as a first step, it emphasizes that the impact of small-scale hydrodynamic patterns should not be entirely neglected. Potential improvements could involve taking into account different classes of particle sinking velocity as in Picard et al. (2024) and accounting for depth-dependent sinking speeds, incorporating remineralization processes as in Dever et al. (2021).

Secondly, testing different clustering algorithms and increasing the number of input parameters could enhance the clustering results. Additional physical parameters, such as buoyancy gradient, and more depths beyond 200 and 500 m, could be considered. Furthermore, particle trajectory data from higher-resolution circulation simulations would better simulate the scales associated with submesoscale eddies and fronts (Balwada et al., 2021), allowing for a more accurate assessment of their impact on particle distribution variability at depth.

Our study focuses on the variability of physical dynamics within the mesopelagic layer (200–1,000 m) and does not directly address particle flux at depth or sea surface chlorophyll. Future work could relate particle flux in sediment traps to sea surface chlorophyll through particle trajectories (Picard et al., 2024). This approach can incorporate different sinking velocities to represent various particle sizes. Initial particle seeding can be weighted using satellite data (ocean color) or physical-biological model outputs that provide insights into primary production (PP) or surface chlorophyll content. This would allow for the assessment of export flux variability at depth by incorporating some biological activity variability. However, this method does not account for particle size spectra changes due to transformations in the water column, which require consideration of more complex biological processes. Despite these limitations, this approach offers insights into how initial conditions, such as the location of heterogeneous particle sources and initial particle size spectra or sinking velocities—influence particle distribution at depth in terms of physics and PP intensity.

Data Availability Statement

The CROCO ocean model is available at <https://www.croco-ocean.org>. The Lagrangian particle tracking software Pyticles is available at <https://github.com/Mesharou/Pyticles> and has been published on Zenodo at <https://doi.org/10.5281/zenodo.4973786>.

Acknowledgments

This work was supported by the ISblue project, an Interdisciplinary graduate school for the blue planet (ANR-17-EURE-0015), and co-funded by a grant from the French government under the program “Investissements d’Avenir.” This manuscript contributes to the APERO project funded by the National Research Agency under the grant APERO (Grant ANR ANR-21-CE01-0027) and by the French LEFE-Cyber program and to the DEEPER project (Grant ANR-19-CE01-0002-01). XY was supported by National Natural Science Foundation of China (42361144844, 42206002) and Guangdong Basic and Applied Basic Research Foundation (2023A1515010654). Simulations were performed using HPC resources from GENCI-TGCC (Grant 2022-A0090112051) and from DATARMOR of “Pôle de Calcul Intensif pour la Mer” at Ifremer, Brest, France. The authors thank Mathieu Le Corre for providing CROCO simulation outputs.

References

- Allen, J., & Naveira-Garabato, A. (2013). *Rrs discovery cruise 381, 28 Aug-03 Oct 2012. Ocean surface mixing, Ocean submesoscale interaction study (osmosis)*. National Oceanography Centre Southampton.
- Balwada, D., Xiao, Q., Smith, S., Abernathy, R., & Gray, A. (2021). Vertical fluxes conditioned on vorticity and strain reveal submesoscale ventilation. *Journal of Physical Oceanography*, 51(9), 2883–2901. <https://doi.org/10.1175/jpo-d-21-0016.1>
- Bernard, D., Biabiany, E., Cécé, R., Chery, R., & Sekkat, N. (2022). Clustering analysis of the sargassum transport process: Application to beaching prediction in the lesser antilles. *Ocean Science*, 18(4), 915–935. <https://doi.org/10.5194/os-18-915-2022>
- Bidigare, R. R., Benitez-Nelson, C., Leonard, C. L., Quay, P. D., Parsons, M. L., Foley, D. G., & Seki, M. P. (2003). Influence of a cyclonic eddy on microheterotroph biomass and carbon export in the lee of Hawaii. *Geophysical Research Letters*, 30(6). <https://doi.org/10.1029/2002gl16393>
- Boyd, P., Claustre, H., Levy, M., Siegel, D., & Weber, T. (2019). Multi-faceted particle pumps drive carbon sequestration in the ocean. *Nature*, 568(7752), 327–335. <https://doi.org/10.1038/s41586-019-1098-2>
- Buesseler, K. O., Antia, A., Chen, M., Fowler, S. W., Gardner, W. D., Gustafsson, O., et al. (2007). An assessment of the use of sediment traps for estimating upper ocean particle fluxes. *Journal of Marine Research*, 65(3), 345–416. <https://doi.org/10.1357/002224007781567621>
- Buesseler, K. O., Lamborg, C., Cai, P., Escoube, R., Johnson, R., Pike, S., et al. (2008). Particle fluxes associated with mesoscale eddies in the Sargasso Sea. *Deep Sea Research Part II: Topical Studies in Oceanography*, 55(10–13), 1426–1444. <https://doi.org/10.1016/j.dsr2.2008.02.007>
- Callies, J., Barkan, R., & Garabato, A. N. (2020). Time scales of submesoscale flow inferred from a mooring array. *Journal of Physical Oceanography*, 50(4), 1065–1086. <https://doi.org/10.1175/jpo-d-19-0254.1>
- Callies, J., Ferrari, R., Klymak, J. M., & Gula, J. (2015). Seasonality in submesoscale turbulence. *Nature Communications*, 6(1), 6862. <https://doi.org/10.1038/ncomms7862>
- Chelton, D. B., DeSzoeke, R. A., Schlax, M. G., El Naggar, K., & Siwertz, N. (1998). Geographical variability of the first baroclinic rossby radius of deformation. *Journal of Physical Oceanography*, 28(3), 433–460. [https://doi.org/10.1175/1520-0485\(1998\)028<0433:gvotfb>2.0.co;2](https://doi.org/10.1175/1520-0485(1998)028<0433:gvotfb>2.0.co;2)
- Chen, K., Gaube, P., & Pallàs-Sanz, E. (2020). On the vertical velocity and nutrient delivery in warm core rings. *Journal of Physical Oceanography*, 50(6), 1557–1582. <https://doi.org/10.1175/jpo-d-19-0239.1>
- Conte, M. H., Ralph, N., & Ross, E. H. (2001). Seasonal and interannual variability in deep ocean particle fluxes at the oceanic flux program (OFP)/Bermuda Atlantic time series (bats) site in the western Sargasso Sea near Bermuda. *Deep Sea Research Part II: Topical Studies in Oceanography*, 48(8–9), 1471–1505. [https://doi.org/10.1016/s0967-0645\(00\)00150-8](https://doi.org/10.1016/s0967-0645(00)00150-8)
- D’Asaro, E., Shcherbina, A., Klymak, J., Molemaker, J., Novelli, G., Guigand, C., et al. (2018). Ocean convergence and the dispersion of flotsam. *Proceedings of the National Academy of Sciences*, 115(6), 1162–1167. <https://doi.org/10.1073/pnas.1718453115>
- Deuser, W., & Ross, E. (1980). Seasonal change in the flux of organic carbon to the deep Sargasso Sea. *Nature*, 283(5745), 364–365. <https://doi.org/10.1038/283364a0>
- Deuser, W., Ross, E., & Anderson, R. (1981). Seasonality in the supply of sediment to the deep Sargasso Sea and implications for the rapid transfer of matter to the deep ocean. *Deep-Sea Research, Part A: Oceanographic Research Papers*, 28(5), 495–505. [https://doi.org/10.1016/0198-0149\(81\)90140-0](https://doi.org/10.1016/0198-0149(81)90140-0)
- Dever, M., Nicholson, D., Omand, M., & Mahadevan, A. (2021). Size-differentiated export flux in different dynamical regimes in the ocean. *Global Biogeochemical Cycles*, 35(3). <https://doi.org/10.1029/2020gb006764>
- d’Ovidio, F., De Monte, S., Alvain, S., Dandonneau, Y., & Lévy, M. (2010). Fluid dynamical niches of phytoplankton types. *Proceedings of the National Academy of Sciences*, 107(43), 18366–18370. <https://doi.org/10.1073/pnas.1004620107>
- Emerson, S. (2014). Annual net community production and the biological carbon flux in the ocean. *Global Biogeochemical Cycles*, 28(1), 14–28. <https://doi.org/10.1002/2013gb004680>
- Estapa, M., Feen, M., & Breves, E. (2019). Direct observations of biological carbon export from profiling floats in the subtropical North Atlantic. *Global Biogeochemical Cycles*, 33(3), 282–300. <https://doi.org/10.1029/2018gb006098>
- Guidi, L., Calil, P. H., Duhamel, S., Björkman, K. M., Doney, S. C., Jackson, G. A., et al. (2012). Does eddy-eddy interaction control surface phytoplankton distribution and carbon export in the north pacific subtropical gyre? *Journal of Geophysical Research*, 117(G2). <https://doi.org/10.1029/2012jg001984>

- Guidi, L., Stemann, L., Legendre, L., Picheral, M., Prieur, L., & Gorsky, G. (2007). Vertical distribution of aggregates ($110 > \mu\text{m}$) and mesoscale activity in the northeastern Atlantic: Effects on the deep vertical export of surface carbon. *Limnology & Oceanography*, *52*(1), 7–18. <https://doi.org/10.4319/lo.2007.52.1.0007>
- Gula, J., & Collin, J. (2021). Pyticles: A Python/Fortran hybrid parallelized code for 3D Lagrangian particles advection using ROMS/CROCO model data. *Zenodo*. <https://doi.org/10.5281/zenodo.4973786>
- Hartman, S. E., Lampitt, R. S., Larkin, K. E., Pagnani, M., Campbell, J., Gkritzalis, T., et al. (2012). The porcupine Abyssal Plain fixed-point sustained observatory (pap-so): Variations and trends from the Northeast Atlantic fixed-point time-series. *ICES Journal of Marine Science*, *69*(5), 776–783. <https://doi.org/10.1093/icesjms/iss077>
- Hisaki, Y. (2013). Classification of surface current maps. *Deep Sea Research Part I: Oceanographic Research Papers*, *73*, 117–126. <https://doi.org/10.1016/j.dsr.2012.12.001>
- Honjo, S. (1982). Seasonality and interaction of biogenic and lithogenic particulate flux at the Panama basin. *Science*, *218*(4575), 883–884. <https://doi.org/10.1126/science.218.4575.883>
- Hosegood, P., Nightingale, P., Rees, A., Widdicombe, C., Woodward, E., Clark, D., & Torres, R. (2017). Nutrient pumping by submesoscale circulations in the Mauritanian upwelling system. *Progress in Oceanography*, *159*, 223–236. <https://doi.org/10.1016/j.poccean.2017.10.004>
- Huffard, C. L., Durkin, C. A., Wilson, S. E., McGill, P. R., Henthorn, R., & Smith Jr, K. L. (2020). Temporally-resolved mechanisms of deep-ocean particle flux and impact on the seafloor carbon cycle in the northeast pacific. *Deep Sea Research Part II: Topical Studies in Oceanography*, *173*, 104763. <https://doi.org/10.1016/j.dsr2.2020.104763>
- Jolliffe, I. T. (2002). *Principal component analysis for special types of data*. Springer.
- Jouandet, M.-P., Jackson, G. A., Carlotti, F., Picheral, M., Stemann, L., & Blain, S. (2014). Rapid formation of large aggregates during the spring bloom of Kerguelen Island: Observations and model comparisons. *Biogeosciences*, *11*(16), 4393–4406. <https://doi.org/10.5194/bg-11-4393-2014>
- Kaiser, H. F. (1960). The application of electronic computers to factor analysis. *Educational and Psychological Measurement*, *20*(1), 141–151. <https://doi.org/10.1177/001316446002000116>
- Kemp, A. E., Pearce, R. B., Grigorov, I., Rance, J., Lange, C., Quilty, P., & Salter, I. (2006). Production of giant marine diatoms and their export at oceanic frontal zones: Implications for SI and C flux from stratified oceans. *Global Biogeochemical Cycles*, *20*(4). <https://doi.org/10.1029/2006gb002698>
- Klein, P., & Lapeyre, G. (2009). The oceanic vertical pump induced by mesoscale and submesoscale turbulence. *Annual Review of Marine Science*, *1*, 351–375. <https://doi.org/10.1146/annurev.marine.010908.163704>
- Lampitt, R. S., Briggs, N., Cael, B., Espinola, B., Hélaouët, P., Henson, S. A., et al. (2023). Deep ocean particle flux in the Northeast Atlantic over the past 30 years: Carbon sequestration is controlled by ecosystem structure in the upper ocean. *Frontiers in Earth Science*, *11*, 1176196. <https://doi.org/10.3389/feart.2023.1176196>
- Le Corre, M., Gula, J., & Tréguier, A.-M. (2020). Barotropic vorticity balance of the north Atlantic subpolar gyre in an eddy-resolving model. *Ocean Science*, *16*(2), 451–468. <https://doi.org/10.5194/os-16-451-2020>
- Lévy, M., Ferrari, R., Franks, P., Martin, A., & Rivière, P. (2012). Bringing physics to life at the submesoscale. *Geophysical Research Letters*, *39*(14), L14602. <https://doi.org/10.1029/2012gl052756>
- Mahadevan, A. (2016). The impact of submesoscale physics on primary productivity of plankton. *Annual Review of Marine Science*, *8*(1), 161–184. <https://doi.org/10.1146/annurev-marine-010814-015912>
- Mahadevan, A., & Archer, D. (2000). Modeling the impact of fronts and mesoscale circulation on the nutrient supply and biogeochemistry of the upper ocean. *Journal of Geophysical Research*, *105*(C1), 1209–1225. <https://doi.org/10.1029/1999jc900216>
- Mahadevan, A., & Tandon, A. (2006). An analysis of mechanisms for submesoscale vertical motion at ocean fronts. *Ocean Modelling*, *14*(3–4), 241–256. <https://doi.org/10.1016/j.ocemod.2006.05.006>
- McGillicuddy, D. J. (2016). Mechanisms of physical-biological-biogeochemical interaction at the oceanic mesoscale. *Annual Review of Marine Science*, *8*(1), 125–159. <https://doi.org/10.1146/annurev-marine-010814-015606>
- McGillicuddy, D. J., Resplandy, L., & Lévy, M. (2019). Estimating particle export flux from satellite observations: Challenges associated with spatial and temporal decoupling of production and export. *Journal of Marine Research*, *77*(2), 247–258. <https://doi.org/10.1357/002224019828474331>
- McWilliams, J. C., Graves, L. P., & Montgomery, M. T. (2003). A formal theory for vortex rossby waves and vortex evolution. *Geophysical & Astrophysical Fluid Dynamics*, *97*(4), 275–309. <https://doi.org/10.1080/0309192031000108698>
- Nardelli, B. B. (2013). Vortex waves and vertical motion in a mesoscale cyclonic eddy. *Journal of Geophysical Research: Oceans*, *118*(10), 5609–5624. <https://doi.org/10.1002/jgrc.20345>
- Naveira Garabato, A. C., Yu, X., Callies, J., Barkan, R., Polzin, K. L., Frajka-Williams, E. E., et al. (2022). Kinetic energy transfers between mesoscale and submesoscale motions in the open ocean's upper layers. *Journal of Physical Oceanography*, *52*(1), 75–97. <https://doi.org/10.1175/jpo-d-21-0099.1>
- Nowicki, M., DeVries, T., & Siegel, D. A. (2022). Quantifying the carbon export and sequestration pathways of the ocean's biological carbon pump. *Global Biogeochemical Cycles*, *36*(3), e2021GB007083. <https://doi.org/10.1029/2021gb007083>
- Omand, M. M., D'Asaro, E. A., Lee, C. M., Perry, M. J., Briggs, N., Cetinić, I., & Mahadevan, A. (2015). Eddy-driven subduction exports particulate organic carbon from the spring bloom. *Science*, *348*(6231), 222–225. <https://doi.org/10.1126/science.1260062>
- Picard, T., Baker, C. A., Gula, J., Fablet, R., Mémyer, L., & Lampitt, R. (2024). Estimating the variability of deep ocean particle flux collected by sediment traps using satellite data and machine learning. *EGU Sphere*, *2024*, 1–32.
- Pilo, G. S., Oke, P. R., Coleman, R., Rykova, T., & Ridgway, K. (2018). Patterns of vertical velocity induced by eddy distortion in an ocean model. *Journal of Geophysical Research: Oceans*, *123*(3), 2274–2292. <https://doi.org/10.1002/2017jc013298>
- Qiu, B., Scott, R. B., & Chen, S. (2008). Length scales of eddy generation and nonlinear evolution of the seasonally modulated south pacific subtropical countercurrent. *Journal of Physical Oceanography*, *38*(7), 1515–1528. <https://doi.org/10.1175/2007jpo3856.1>
- Resplandy, L., Lévy, M., & McGillicuddy, D. J., Jr. (2019). Effects of eddy-driven subduction on ocean biological carbon pump. *Global Biogeochemical Cycles*, *33*(8), 1071–1084. <https://doi.org/10.1029/2018gb006125>
- Riley, J., Sanders, R., Marsay, C., Le Moigne, F., Achterberg, E., & Poulton, A. (2012). The relative contribution of fast and slow sinking particles to ocean carbon export: Export of fast and slow sinking poc. *Global Biogeochemical Cycles*, *26*(1). <https://doi.org/10.1029/2011gb004085>
- Rocha, C. B., Gille, S. T., Chereskin, T. K., & Menemenlis, D. (2016). Seasonality of submesoscale dynamics in the kuroshio extension. *Geophysical Research Letters*, *43*(21), 11–304. <https://doi.org/10.1002/2016gl071349>
- Ruhl, H. A., Bahr, F. L., Henson, S. A., Hosking, W. B., Espinola, B., Kahru, M., et al. (2020). Understanding the remote influences of ocean weather on the episodic pulses of particulate organic carbon flux. *Deep Sea Research Part II: Topical Studies in Oceanography*, *173*, 104741. <https://doi.org/10.1016/j.dsr2.2020.104741>

- Sayre, R. G., Wright, D. J., Breyer, S. P., Butler, K. A., Graafland, K. V., Costello, M. J., et al. (2017). A three-dimensional mapping of the ocean based on environmental data. *Oceanography*, *30*(1), 90–103. <https://doi.org/10.5670/oceanog.2017.116>
- Schubert, R., Gula, J., Greatbatch, R. J., Baschek, B., & Biastoch, A. (2020). The submesoscale kinetic energy cascade: Mesoscale absorption of submesoscale mixed layer eddies and frontal downscale fluxes. *Journal of Physical Oceanography*, *50*(9), 2573–2589. <https://doi.org/10.1175/jpo-d-19-0311.1>
- Schubert, R., Vergara, O., & Gula, J. (2023). The open ocean kinetic energy cascade is strongest in late winter and spring. *Communications Earth & Environment*, *4*(1), 450. <https://doi.org/10.1038/s43247-023-01111-x>
- Shchepetkin, A. F., & McWilliams, J. C. (2005). The regional oceanic modeling system (ROMS): A split-explicit, free-surface, topography-following-coordinate oceanic model. *Ocean Modelling*, *9*(4), 347–404. <https://doi.org/10.1016/j.ocemod.2004.08.002>
- Shcherbina, A. Y., D'Asaro, E. A., Lee, C. M., Klymak, J. M., Molemaker, M. J., & McWilliams, J. C. (2013). Statistics of vertical vorticity, divergence, and strain in a developed submesoscale turbulence field. *Geophysical Research Letters*, *40*(17), 4706–4711. <https://doi.org/10.1002/grl.50919>
- Siegel, D., Buesseler, K., Doney, S. C., Sailley, S., Behrenfeld, M. J., & Boyd, P. (2014). Global assessment of ocean carbon export by combining satellite observations and food-web models. *Global Biogeochemical Cycles*, *28*(3), 181–196. <https://doi.org/10.1002/2013gb004743>
- Siegel, D., & Deuser, W. (1997). Trajectories of sinking particles in the sargasso sea: Modeling of statistical funnels above deep-ocean sediment traps. *Deep Sea Research Part I: Oceanographic Research Papers*, *44*(9–10), 1519–1541. [https://doi.org/10.1016/s0967-0637\(97\)00028-9](https://doi.org/10.1016/s0967-0637(97)00028-9)
- Siegel, D., Fields, E., & Buesseler, K. (2008). A bottom-up view of the biological pump: Modeling source funnels above ocean sediment traps. *Deep Sea Research Part I: Oceanographic Research Papers*, *55*(1), 108–127. <https://doi.org/10.1016/j.dsr.2007.10.006>
- Siegel, D., Granata, T., Michaels, A., & Dickey, T. (1990). Mesoscale eddy diffusion, particle sinking, and the interpretation of sediment trap data. *Journal of Geophysical Research*, *95*(C4), 5305–5311. <https://doi.org/10.1029/jc095ic04p05305>
- Smilenova, A., Gula, J., Le Corre, M., Houpert, L., & Reecht, Y. (2020). A persistent deep anticyclonic vortex in the rockall trough sustained by anticyclonic vortices shed from the slope current and wintertime convection. *Journal of Geophysical Research: Oceans*, *125*(10), e2019JC015905. <https://doi.org/10.1029/2019JC015905>
- Smith, K. L., Jr., Ruhl, H. A., Huffard, C. L., Messié, M., & Kahru, M. (2018). Episodic organic carbon fluxes from Surface Ocean to abyssal depths during long-term monitoring in ne pacific. *Proceedings of the National Academy of Sciences*, *115*(48), 12235–12240. <https://doi.org/10.1073/pnas.1814559115>
- Sun, Q., Little, C. M., Barthel, A. M., & Padman, L. (2021). A clustering-based approach to ocean model–data comparison around Antarctica. *Ocean Science*, *17*(1), 131–145. <https://doi.org/10.5194/os-17-131-2021>
- Taylor, J. R., & Ferrari, R. (2011). Ocean fronts trigger high latitude phytoplankton blooms. *Geophysical Research Letters*, *38*(23). <https://doi.org/10.1029/2011gl049312>
- Villa-Alfageme, M., de Soto, F., Le Moigne, F. A. C., Giering, S. L. C., Sanders, R., & García-Tenorio, R. (2014). Observations and modeling of slow-sinking particles in the twilight zone. *Global Biogeochemical Cycles*, *28*(11), 1327–1342. <https://doi.org/10.1002/2014gb004981>
- Wang, L., Gula, J., Collin, J., & Mémerly, L. (2022). Effects of mesoscale dynamics on the path of fast-sinking particles to the deep ocean: A modeling study. *Journal Of Geophysical Research-oceans*, *127*(7). <https://doi.org/10.1029/2022jc018799>
- Waniek, J., Koeve, W., & Prien, R. (2000). Trajectories of sinking particles and the catchment areas above sediment traps in the northeast atlantic. *Journal of Marine Research*, *58*(6), 983–1006. <https://doi.org/10.1357/002224000763485773>
- Waniek, J., Schulz-Bull, D. E., Blanz, T., Prien, R. D., Oschlies, A., & Müller, T. J. (2005). Interannual variability of deep water particle flux in relation to production and lateral sources in the northeast atlantic. *Deep Sea Research Part I: Oceanographic Research Papers*, *52*(1), 33–50. <https://doi.org/10.1016/j.dsr.2004.08.008>
- Wunsch, C. (1998). The work done by the wind on the oceanic general circulation. *Journal of Physical Oceanography*, *28*(11), 2332–2340. [https://doi.org/10.1175/1520-0485\(1998\)028<2332:twdbtw>2.0.co;2](https://doi.org/10.1175/1520-0485(1998)028<2332:twdbtw>2.0.co;2)
- Yu, X., Barkan, R., & Naveira Garabato, A. C. (2024). Intensification of submesoscale frontogenesis and forward energy cascade driven by upper-ocean convergent flows. *Nature Communications*, *15*(1), 9214. <https://doi.org/10.1038/s41467-024-53551-4>
- Yu, X., Naveira Garabato, A. C., Martin, A. P., Gwyn Evans, D., & Su, Z. (2019). Wind-forced symmetric instability at a transient mid-ocean front. *Geophysical Research Letters*, *46*(20), 11281–11291. <https://doi.org/10.1029/2019gl084309>
- Yu, X., Naveira Garabato, A. C., Martin, A. P., Buckingham, C. E., Brannigan, L., & Su, Z. (2019). An annual cycle of submesoscale vertical flow and restratification in the upper ocean. *Journal of Physical Oceanography*, *49*(6), 1439–1461. <https://doi.org/10.1175/jpo-d-18-0253.1>
- Zhang, X., Yu, X., Ponte, A. L., Caspar-Cohen, Z., Le Gentil, S., Wang, L., & Gong, W. (2024). Lagrangian versus Eulerian spectral estimates of surface kinetic energy over the global ocean. *Journal of Geophysical Research: Oceans*, *129*(8), e2024JC021057. <https://doi.org/10.1029/2024jc021057>
- Zhang, Z., & Qiu, B. (2020). Surface chlorophyll enhancement in mesoscale eddies by submesoscale spiral bands. *Geophysical Research Letters*, *47*(14), e2020GL088820. <https://doi.org/10.1029/2020gl088820>
- Zhou, K., Dai, M., Xiu, P., Wang, L., Hu, J., & Benitez-Nelson, C. R. (2020). Transient enhancement and decoupling of carbon and opal export in cyclonic eddies. *Journal of Geophysical Research: Oceans*, *125*(9), e2020JC016372. <https://doi.org/10.1029/2020jc016372>